Silk Nanoparticles for Combinational Anti-Cancer Chemo and Photothermal Therapy

M.Sc. Thesis

By
MOUMITA PAL

DEPARTMENT OF BIOSCIENCES AND BIOMEDICAL ENGINEERING
INDIAN INSTITUTE OF TECHNOLOGY INDORE
MAY 2024

Silk Nanoparticles for Combinational Anti-Cancer Chemo and Photothermal Therapy

A THESIS

Submitted in partial fulfillment of the requirements for the award of the degree
of
Master of Science

by
MOUMITA PAL

DEPARTMENT OF BIOSCIENCES AND BIOMEDICAL ENGINEERING
INDIAN INSTITUTE OF TECHNOLOGY INDORE
MAY 2024

INDIAN INSTITUTE OF TECHNOLOGY INDORE

CANDIDATE'S DECLARATION

I hereby certify that the work which is being presented in the thesis entitled **SILK NANOPARTICLES FOR COMBINATIONAL ANTI-CANCER CHEMO AND PHOTOTHERMAL THERAPY** in the partial fulfilment of the requirements for the award of the degree of **MASTER OF SCIENCE** and submitted in the **DEPARTMENT OF BIOSCIENCES AND BIOMEDICAL ENGINEERING, Indian Institute of Technology Indore**, is an authentic record of my own work carried out during the time period from July 2022 to May 2024 under the supervision of Dr. Sharad Gupta, Associate Professor.

The matter presented in this thesis has not been submitted by me for the award of any other degree of this or any other institute.

Moumita Pal 24/5/2024

Signature of the student with date
Moumita Pal

This is to certify that the above statement made by the candidate is correct to the best of my/our knowledge.

Sharad Gupta 24 May 2024

Signature of M.Sc. Thesis supervisor
Dr. Sharad Gupta

MOUMITA PAL has successfully given her M.Sc. Oral Examination which was held on **10TH MAY 2024.**

Sharad Gupta 24 May 2024

Signature(s) of Supervisor(s) of MSc thesis
Date:

P.V. Kodgire

DPGC Convener,
Date: 24/05/2024

ACKNOWLEDGEMENTS

I am profoundly grateful to my thesis supervisor, **Dr. Sharad Gupta,** for his invaluable guidance, support, and encouragement throughout my research journey. His expertise, insightful feedback, and unwavering patience have been instrumental in the completion of this thesis. He has not only provided me with the academic mentorship necessary to navigate the complexities of my research but also fostered an environment of intellectual curiosity and innovation. His dedication to my development as a researcher has been truly inspiring, and their constructive criticism has significantly enhanced the quality of my work.

I am highly obliged to **Dr. Abhijit Joshi** for allowing me to use the ultrasonic atomizer machine for fabricating silk nanoparticles which is a very important part of my thesis.

I am thankful to the **M.Sc. coordinator**, **DPGC Convenor**, **Head of the Department,** and **BSBE office staff** for their administrative support and for fostering a stimulating academic environment that encouraged intellectual exploration and scholarly pursuits.

I am also grateful to the **SIC staff** for helping me in my experiments which involved the use of sophisticated instruments such as a Scanning electron microscope (SEM), Circular Dichroism (CD), etc.

I am grateful to **DBT** for granting me the fellowship for 2 years and helping in my research journey.

My heartfelt appreciation goes to each member of my research lab. I am obliged to **Dr. Saumya Jaiswal** for assisting me with this project. I am grateful to **Ms. Priyanka Payal** for constantly supporting me in every experimental procedure, not only you helped me in my research but also guided me well for my future plans. I am thankful to **Ms. Anusha Srivastava, Dr. Pankaj Kumar, Ms. Vibha Choudhary, Mr. Neeraj Sati, Mr. Advait Sohani** and **Mr. Surjyapratap Sarange**. Their collaborative spirit, constructive discussions, and shared passion for

scientific inquiry have significantly contributed to the quality and depth of this thesis. I am thankful to **Mr. Badri Sahoo** and **Ms. Simran Rana** for helping me in the fabrication of silk nanoparticles which is the basis of my thesis. I would also like to thank neighboring lab members **Ms. Pallabi Seal, Ms. Sangeeta Shrivas, Ms. Ritika Sharma, and Ms. Harshita Samaur** for their constant support.

I am grateful to my friends, seniors, and juniors whose camaraderie, encouragement, and shared experiences have been invaluable. I am obliged to **Mr. Mallar Dasgupta, Ms. Sukanya Samanta, Mr. Aritra Chakraborty, Ms. Swagata Laksmi Dhali, Ms. Sampurna Dasgupta, Mr. Sugato Panda, Mr. Sagnik Mitra and Mr. Ritabrata Sikdar.** Their support and guidance, both academically and personally, have made this journey more fulfilling and enriching. I am thankful to **Mr. Debanjan Bagchi** for helping me in the TCS-PC experiment.

To my beloved parents **Mr. Manash Ranjan Pal** and **Mrs. Krishna Pal**, I owe a debt of gratitude beyond words. Their unwavering belief in my abilities, endless encouragement, and sacrifices have been the foundation of my academic achievements. Their love and support have been my driving force, motivating me to strive for excellence.

Lastly, I acknowledge the divine blessings and guidance of **God**. His grace has been a constant source of strength, resilience, and inspiration, guiding me through challenges and illuminating my path toward academic and personal growth.

Moumita Pal

This thesis is dedicated to my family, friends, seniors, and my beloved juniors.

Abstract

Cancer is one of the deadliest diseases in the world but conventional cancer treatments have several side effects. Therefore, photothermal therapy is an effective alternative solution due to the localized thermal effect which makes it suitable for solid tumors. This study explores biocompatible silk fibroin nanoparticles for simultaneous delivery of Doxorubicin (DOX) and Indocyanine Green (ICG) for combinational chemo and photothermal therapy. Efficient encapsulation of ICG, induced by DOX-mediated J-aggregation, was achieved in ICG -DOX loaded silk nanoparticles (IDSNPs) (~98%), surpassing the loading capacities of only ICG-loaded nanoparticles (ISNPs) (~20%). The enhanced loading of ICG within IDSNPs might be due to the interaction of ICG and DOX with the silk nanoparticles which was confirmed using circular dichroism spectroscopy.. IDSNPs exhibited increased size (~80±4 nm) compared to ISNPs and showed enhanced photothermal stability compared to free ICG. Cellular studies have demonstrated the superior efficacy of ICG-Loaded Silk Nanoparticles (IDSNPs) compared to free Doxorubicin (DOX) in terms of cytotoxicity and cellular uptake. The IC50 value of IDSNPs was found to be 0.6725 ± 0.02 µM, which is significantly lower than that of free DOX, which had an IC50 value of 1.15 ± 0.02 µM. This indicates that IDSNPs are more effective at inhibiting cell growth at lower concentrations. Moreover, IDSNPs exhibited preferential cellular uptake, which enhances their cytotoxic potential. This effect was particularly pronounced following laser irradiation. The combination of IDSNPs and laser treatment resulted in a significant decrease in cell viability, with only 30% of the cells remaining viable within 6 hours post-irradiation. This highlights the potential of IDSNPs for use in targeted cancer therapy, as they not only improve the delivery and efficacy of chemotherapeutic agents but also enhance the

therapeutic outcomes through synergistic effects with photothermal therapy. This demonstrates IDSNPs' potential in targeted cancer therapy, improving drug delivery and therapeutic outcomes. This study underscores IDSNPs' dual role as effective chemotherapeutic and photothermal agents, offering synergistic therapeutic benefits for advanced cancer treatment.

TABLE OF CONTENTS

LIST OF FIGURES

LIST OF TABLES

ACRONYMS

DOX	Doxorubicin
ICG	Indocyanine Green
FDA	Food and Drug Administration of America
PTT	Photothermal therapy
DMEM	Dulbecco's Modified Eagle Medium
FBS	Fetal Bovine Serum
PBS	Phosphate Buffer Saline
TCS-PC	Time -Correlated Single Photon Counting
MTT	3-(4,5-dimethylthiazol-2-yl)-2,5-diphenyl tetrazolium bromide
PI	Propidium Iodide
NIR	Near Infrared Radiation
MRI	Magnetic Resonance Imaging
CT-SCAN	Computed tomography
MDR	Multi-Drug resistance
DMSO	Dimethyl sulfoxide
SNP	Silk nanoparticles
ISNP	ICG-loaded silk nanoparticles
IDSNP	ICG and DOX loaded silk nanoparticles

Chapter 1

Introduction

Cancer is a complicated and varied illness, rarely discovered in its early stages (Chandrashekar et al., 2022).Cancer is a multi-faceted disease that causes malignant tumors by altering the cellular physiology in several different ways.At its biological end stage, the condition leads to abnormal cell growth, commonly referred to as neoplasia.. Mortality and morbidity for the majority of cancer patients are caused by tumor cell invasion of neighboring tissues and distant organs (Seyfried & Shelton, 2010). Cancer is a global public health concern and the second most significant cause of death in the US (Siegel et al., 2023).

Cancer is a highly challenging opponent in the field of human health, causing a substantial worldwide burden because of its widespread occurrence, variety, and intricate characteristics. “According to the WHO, cancers impose the largest worldwide burden (244.6 million DALYs) Disability-Adjusted Life Years (DALYs), both in men (137.4 million DALYs) and in women (107.1 million DALYs) ”(Mattiuzzi & Lippi, 2019).

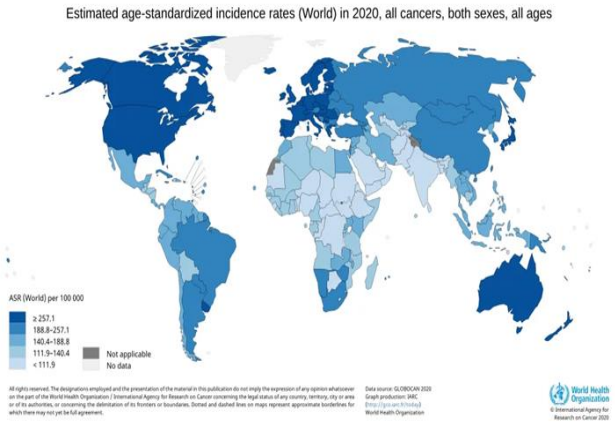

Figure 1.1. *Cancer epidemiology according to GLOBOCAN DATA 2020* (*GLOBOCAN ,2020*)

1.1. Cancer-Diagnosis and Therapy

Cancer is a complex disease that develops over time and causes a widespread lack of control over growth. Surgery, radiation therapy, and chemotherapy were the only alternatives for cancer treatment for a long time, either alone or in combination. However, combinatorial approaches have recently made tremendous strides in improving our understanding of cancer therapeutic progression pathways and their targeting (Debela et al., 2021).

1.1.1. Cancer-Diagnosis

Cancer diagnosis encompasses a variety of methodologies aimed at ascertaining the existence and magnitude of the malignancy. A biopsy to obtain a sample of cells for laboratory analysis may be performed in addition to laboratory tests such as blood tests,

imaging techniques like CT scans and MRIs, as well as a physical examination to identify the presence of tumors. After the diagnosis of cancer is made, the disease progresses through a staging process that determines its extent and whether it has met certain criteria, such as metastasis to lymph nodes or adjacent tissues.

1.1.1.1. Computed tomography (CT) scan

Computerized tomography (CT) scans are helpful in the detection of cancer. Cancer.Net states that computed tomography (CT) scans are utilized for the following purposes: cancer detection, cancer staging, treatment planning, treatment response evaluation, and recurrence monitoring. In order to help doctors see tumors and other abnormalities, the scan captures X-ray pictures from different angles and then combines them into a three-dimensional picture. The addition of contrast dye in CT scans improves their imaging capabilities; these scans are especially helpful for imaging the head, neck, chest, abdomen, pelvis, and limbs. The entire process usually lasts between ten and thirty minutes and causes minimal discomfort. The elimination of image superimposition is a major benefit of tomographic images over plain

films, and it's also a major advantage over traditional X-rays. The use of computed tomography (CT) scans has skyrocketed since their invention, and they are now ubiquitous in the medical industry (Power et al., 2016).

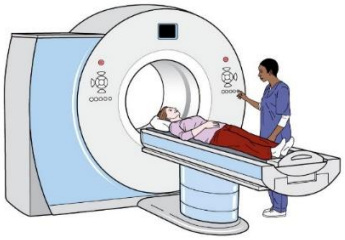

Figure 1.2. *CT scan for cancer diagnosis* (Power et al., 2016)

1.1.1.2. Magnetic resonance imaging (MRI)

A noninvasive medical imaging technique, magnetic resonance imaging (MRI) creates high-resolution pictures of nearly every anatomical and physiological feature within the human body. Unlike X-rays, it does not use ionizing radiation but instead employs magnets and radio waves to generate computer-generated images. By aligning the body's water molecules in one direction and then utilizing a second magnetic field to produce detailed, cross-sectional images of interior organs and structures, an MRI scanner—which is comprised of two powerful magnets—manages to get the job done. One useful technique in the fight against cancer is magnetic resonance imaging, or MRI. It can detect cancers in the body, identify malignant tumors, and provide more information about cancer once detected. In addition to determining the tumor's size and position, MRI helps in the planning and execution of cancer therapies including radiation therapy and surgery, as well as in tracking the efficacy of these interventions. Brain and spinal cord tumors, in particular, are easy to detect and localize with magnetic resonance imaging (MRI),which uses radio waves and powerful magnets to produce comprehensive cross-sectional images of the body. Unlike CT scans, magnetic resonance imaging (MRI) does not involve radiation and is painless and safe to use. It can examine most sections of the body and, in certain cases, produces clearer results than the latter (Haris et al., 2015).

Figure 1.3. *MRI scan for malignant tumor diagnosis* (Haris et al., 2015).

1.1.1.3. Histopathology

A tissue disease examination under a microscope constitutes histopathology, the scientific study of such conditions. Histopathologists assist clinicians in the management of patient care and are tasked with the responsibility of diagnosing tissues. An examination of a biopsy, which involves a small sample of tissue from an organ such as the epidermis, liver, or kidney, can be utilized to arrive at a diagnosis. Histopathologists serve as cancer diagnosticians by analyzing cells and tissues extracted from suspicious nodules and protuberances, determining the characteristics of the anomaly, and furnishing the clinician with pertinent information regarding the ailment. Additionally, histopathology is utilized in scientific inquiry to construct innovative diagnostic techniques and to examine disease processes at the molecular and cellular levels (Knijn et al., 2015).

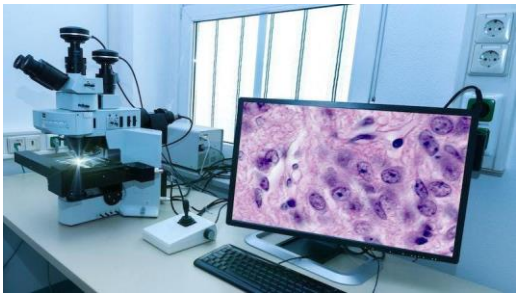

Figure 1.4. *Histopathology for malignant tumor diagnosis* (Knijn et al., 2015)

1.1.2. Conventional Cancer Therapy

1.1.2.1. Surgery

Surgery is a common therapeutic procedure employed in cancer treatment to excise the tumor and adjacent tissue. Surgery, similar to all cancer therapies, possesses benefits, drawbacks, and bad consequences. Potential complications of cancer surgery include bleeding, blood clots, injury to adjacent tissues, adverse drug reactions, and harm to other organs. Discomfort, emesis, and abdominal spasms, Distension of the abdomen until the gastrointestinal system resumes normal activity, Impaired organ function, typically resolve as the patient recovers. Surgery can result in enduring consequences for a patient's physical functionality and overall well-being, in addition to the immediate adverse effects. Postoperative complications such as dehiscence wound or infection, cellulitis, seroma, and nerve damage can raise the likelihood of morbidity (Debela et al., 2021).

1.1.2.2. Chemotherapy

Chemotherapy is a typical cancer treatment that involves the use of medicines to kill cancer cells. However, chemotherapy can create side effects that vary in degree and variety depending on the patient and the type of chemotherapy administered. Some of the most frequent adverse effects of chemotherapy are nausea, decreased appetite, vomiting, changes in taste, exhaustion, hair loss, dry mouth, constipation, bleeding, blood clots, damage to adjacent tissues, medication responses, and organ damage. The severity of these side effects varies based on the patient's health and nutritional status, and chemotherapy side effects are difficult to predict. Patients must disclose any adverse effects they suffer following chemotherapy so that they can receive the necessary assistance and treatment. The management of side effects can increase the efficacy of tumor therapy, and the discovery of new medicines to reduce chemotherapy-induced side effects is required to improve cancer patients' quality of life (Altun & Sonkaya, 2018).

1.1.2.3. Radiation

Radiation therapy is a prevalent cancer treatment that employs high-energy rays to eliminate cancerous cells. Nevertheless, similar to other methods of treating cancer, radiation therapy can induce adverse effects, which may differ in intensity and nature depending on the individual patient and the specific type of radiation therapy employed. The most prevalent adverse effects of radiation therapy are memory or concentration issues, fatigue, skin changes, headache, hair loss, nausea and vomiting, and blurry vision. Radiation therapy may induce both immediate and delayed problems, contingent upon the specific region of the body subjected to treatment. For instance, the adverse effects of radiation on the pelvic region can impact sexual function and fertility in both males and females. Delayed consequences may manifest only after several months or years following the completion of radiation therapy, and their intensity is contingent upon variables such as the dosage of radiation administered, the specific region targeted, and the patient's genetic makeup. Patient engagement in discussing potential difficulties of radiation therapy with their healthcare team and promptly reporting any encountered side effects during and post-treatment is crucial for receiving the necessary support and treatment. Various therapies, including drugs, lifestyle modifications, and emotional support, can effectively address the adverse effects of radiation therapy (Majeed & Gupta, 2024).

Figure 1.5. describes the side effects of conventional cancer therapies such as multidrug resistance in case of chemotherapy, inoperable tumors in case of surgery, inflammation in case of immunotherapy etc.

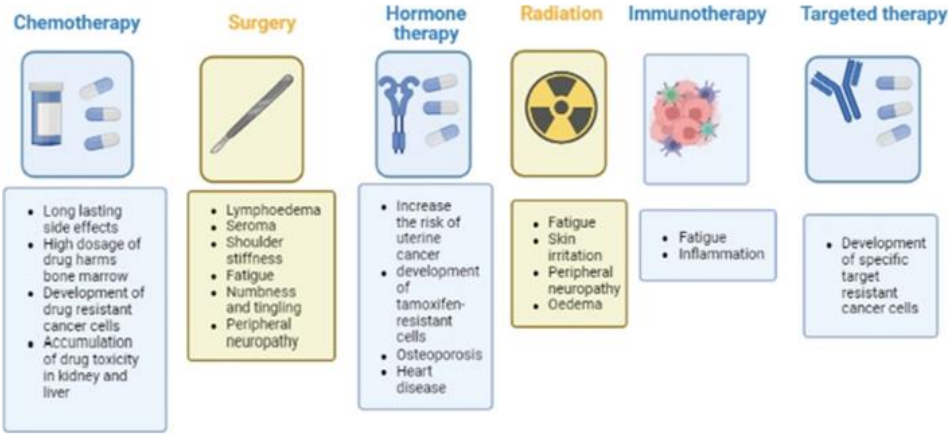

Figure 1.5. *Side effects of conventional cancer treatments* (Barathan et al., 2023)

1.1.3. Photothermal therapy

Photothermal therapy (PTT) is an emerging and promising therapeutic approach that utilizes near-infrared (NIR) laser photo absorbers to produce thermal energy that induces the death of cancer cells (Zou et al., 2016) Figure 1.6.

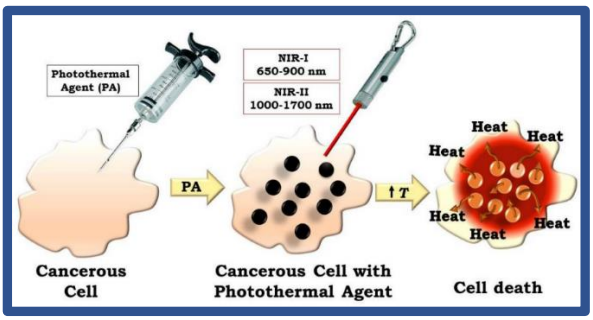

Figure 1.6. *Photothermal therapy to treat cancer cell* (Estelrich & Busquets, 2018) .

Near-infrared (NIR) light is presently the most frequently employed laser in PTT. This is because NIR light exhibits reduced tissue absorption and scattering, thereby facilitating more profound tissue penetration. The wavelength range of light that is designated as NIR is 750–1350 nm. The first and second near-infrared windows (750–1000 nm, NIR-I, and 1000–1350 nm, respectively) may be distinguished within this wavelength range, which is also referred to as the biological window. PTTs that concentrate on NIR-I have a shallow tissue

penetration depth. On the contrary, NIR-II exhibits a more pronounced benefit in PTT due to the ability of light within this spectrum to penetrate deeply into tissues and achieve a greater maximum allowable exposure. In particular, NIR photothermal materials exhibit enhanced therapeutic efficacy and reduced biological interference in deep tissues due to their superior penetration depth in vivo. Moreover, due to their minimal absorption in the NIR wavelength region, biological cells and tissues are impervious to NIR laser damage at low intensities (Huang et al., 2008) According to Figure 1.7. photothermal therapy is an effective process since it is a non /minimally invasive process with precise spatial tempora; selectivity and deep tissue penetration which makes it suitable for solid tumors.

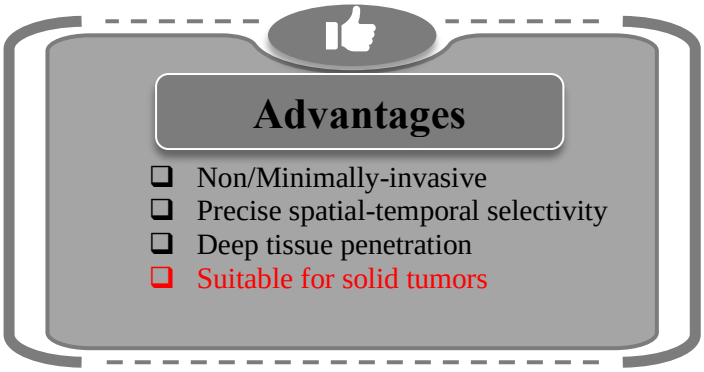

Figure 1.7. *Advantages of Photothermal therapy.*

The primary mechanism underlying the photothermal effect of organic substances is electron transition within molecules. Organic molecules that are exposed to the excitation light will experience absorption, scattering, and transmission, among other processes. A photon transfers its energy to a molecule with which it shares the same energy when the two molecules interact and this results in an electron transition from the ground state to the excited state within the molecule. Internal conversion and vibrational relaxation subsequently transform the molecule into the lowest excited singlet state (S1). There are two main methods by which the molecule can return to its ground state after it has reached the lowest vibration level of S1. The non-radiative transition, like heat generation,

is the alternate path to the ground state, whereas the first path is through fluorescence emission. Non-radiative transitions are commonly used by organic photothermal materials to demonstrate their photothermal action (Li et al., 2021) .Figure 1.8. describes the mechanism of photothermal therapy.

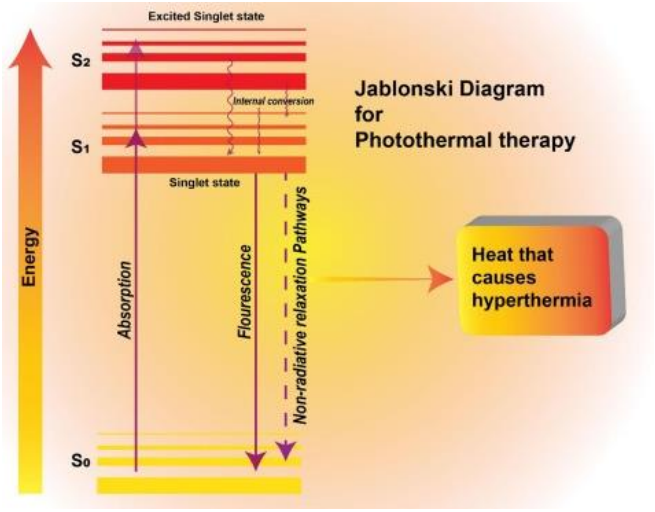

Figure 1.8. *Mechanism of photothermal therapy* (Li et al., 2021).

In the context of PTT applications, the therapeutic temperature range is typically maintained below 50 °C to minimize cell necrosis and inflammation while safeguarding healthy cells from high-temperature environments. When combined with siRNA, miRNA, and other therapeutic technologies, Gold nanorod(GNR)-mediated PTT can substantially enhance antitumor effects, thereby establishing a prospective nontherapeutic field (Zhang et al., 2018) . In case of photothermal therapy the cause of cell death is either due to apoptosis or necrosis according to Figure 1.9.Photothermal Therapy (PTT) is believed to induce apoptosis via the intrinsic mitochondrial pathway as opposed to the extrinsic pathway. In response to cellular stress induced by PTT, Bcl-2 antagonist killer 1 (Bak)and Bcl-2-associated X protein (Bax) are activated, resulting in permeability of the mitochondrial membrane and cytochrome c release. The formation of the apoptosome by Cytochrome c, which subsequently triggers Caspase-9 and Caspase-3, leads to cellular demise. Caspase-8 mediates an interaction between

the extrinsic and intrinsic pathways by converting Bid to tBid, thereby stimulating the intrinsic pathway further(Melamed et al., 2015).

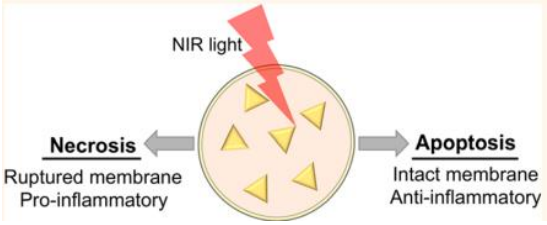

Figure 1.9. *Mechanism of cell death in photothermal therapy* (Melamed et al., 2015)

1.2. Combinational therapies for cancer treatment

Combination therapies have emerged as a promising strategy to overcome the limitations of individual modalities and improve treatment outcomes. One such combination approach is the integration of chemotherapy and photothermal therapy, which has shown promising results in preclinical studies.

Chemotherapy, the prevailing method for treating cancer, continues to encounter obstacles, including drug resistance and undesirable side effects that restrict the highest feasible dosage. During photothermal therapy (PTT), the heating action can enhance the permeability of blood vessels, cell membranes, and extracellular matrix. These physiological changes can enhance the chemotherapeutic impact by augmenting the concentration of anticancer drugs in tumor tissue or metastatic tumor tissue. Furthermore, the concurrent utilization of PTT agents and chemotherapeutic agents can yield synergistic therapeutic outcomes. For instance, chemotherapy can address the issue of light's limited ability to penetrate deeply in PTT and enhance the susceptibility of cancer cells to hyperthermia. Additionally, PTT can heighten the therapeutic responsiveness of multidrug-resistant (MDR) cancer cells. The concurrent use of PTT and chemotherapy can lead to a synergistic effect on hypoxic tumors due to enhanced blood perfusion and oxygen saturation. According to a recent publication, the combination of PTT (photothermal therapy) and chemotherapy using gold-coated nanocages

carrying doxorubicin resulted in a significant decrease in the size of lung metastatic tumors. This reduction was achieved by releasing the medication through hyperthermia-induced mechanisms. In addition, the integration of PTT (photothermal therapy) with chemotherapy through the utilization of polydopamine-coated spiky gold nanoparticles effectively induced immune responses against cancers and eradicated tumors in models of CT26 colon carcinoma and TC-1 lung metastasis (Han & Choi, 2021).

1.3. Protein-based nanoparticles

The protein-based biomacromolecule such as silk fibroin, which is derived from *Bombyx mori*' mulberry silkworms, consists of repeating sequences of six residues named (Gly-Ala-Gly-Ala-Gly-Ser)n repeats, totaling 5507 amino acid repeats. A single disulfide bond connects the heavy (395 kDa) and light (25 kDa) chains of the heterodimeric protein known as biopolymer between residues 172 and 20 (twenty residues from the c terminus) on the L-chain and the H-chain, respectively (Xiao et al., 2016) .Figure 1.10. shows the secondary structure of silk fibroin protein.The secondary structure of silk fibroin is predominantly composed of β-sheets. These β-sheets are formed by hydrogen bonds between the backbone amide and carbonyl groups of the amino acids. The β-sheets are stacked together in an anti-parallel arrangement, creating crystalline regions that provide strength and stability.Silk is a potential nanomaterial for controlled drug release due to its biocompatibility, strong mechanical capabilities, adjustable biodegradation for controlled drug release, usefulness in drug stability, and aqueous-based production and processing possibilities for drug loading. It is possible to modify the secondary structure of silk sequences to control the release of bioactive compounds from silk nanoparticles by regulating the enzymatic breakdown rates of such delivery systems (Numata et al., 2012).

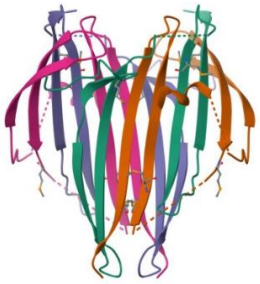

Figure 1.10. *Structure of Silk Fibroin (PDB ID:3UA0).*

1.4. Doxorubicin (DOX)

Doxorubicin, an anthracycline antibiotic derived from natural sources, is among the most efficacious chemotherapy agents employed to treat solid tumors across various forms of cancer (Taymaz-Nikerel et al., 2018). The chemotherapeutic drug doxorubicin, also known as Adriamycin, is orange to red (at neutral pH), water-soluble, and photosensitive. It was obtained from Streptomyces peucetius var. caesius. Dox has been approved by the FDA in 1974. It is often used as the first treatment for a wide range of solid and metastatic tumors, including neuroblastoma, breast, gastric, thyroid, osteogenic bone tumors small cell lung, acute lymphoblastic/myeloblastic leukemia ovarian, bladder, Wilmʿ tumor, Hodgkin's lymphoma, and cutaneous T cell lymphoma (Sritharan & Sivalingam, 2021).

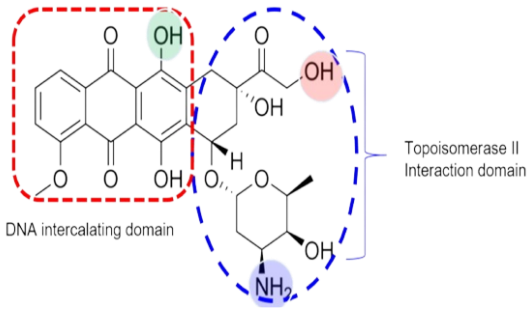

Figure 1.11. *Structure of Doxorubicin* (Sritharan & Sivalingam, 2021)

Doxorubicin exerts its anticancer effects through multiple mechanisms, as proposed by several theories. One mechanism posits that doxorubicin functions by intercalating into DNA molecules, thereby impeding DNA repair processes crucially regulated by topoisomerase II. This inhibition of topoisomerase II activity by doxorubicin disrupts the enzyme's role

in DNA transcription, leading to the interference of DNA recombination within the double-stranded structure and halting DNA replication processes. Additionally, doxorubicin may induce the generation of free radicals, which have the potential to inflict DNA damage, ultimately triggering cell death pathways in cancer cells (Taymaz-Nikerel et al., 2018).

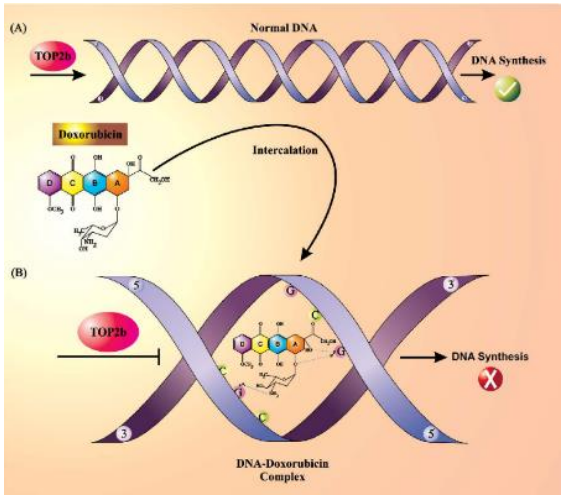

Figure 1.12. *Mechanism of action of Doxorubicin* (Sritharan & Sivalingam, 2021)

1.5. Indocyanine green (ICG)

When excited by near-infrared light, ICG, a tricarbocyanine dye, fluoresces, or gives off light. Many molecules of ICG can dissolve in water, and it bind to β-lipoproteins, especially albumin. Because lymph has a lot of proteins, ICG builds up in the lymphatic channels and lymph nodes. Lymph nodes that have been treated with ICG can be seen 5 minutes after being excited by light and for about 60 minutes after that. ICG has a plasma half-life of 3–4 minutes, and it is eliminated by the liver (Hackethal et al., 2018). Figure 1.13 shows the chemical structure of ICG.

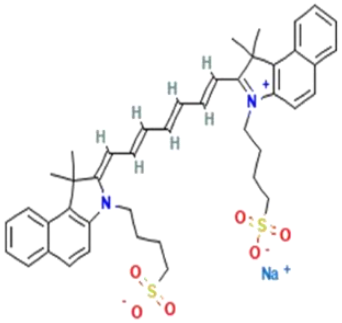

Figure 1.13. *Structure of Indocyanine green (ICG)(Changalvaie et al., 2019).*

Free ICG has two peaks in aqueous solutions: the dimer band (H-peak) at 720 nm and the monomer band (M-peak) at 780 nm on the same wavelength. Even at very high ICG concentrations, there is increased absorption at the 720 nm dimer peak (H-peak) due to the rapid on-top stacking aggregation of ICG molecules. Head-to-tail stacking, as shown by a new peak at 896 nm, has been previously reported to result from heating higher quantities of ICG at greater temperatures. In place of the typical aggregation peak at 720 nm, these aggregates create a J-peak, but in a highly ordered orientation. Extended NIR excitation and superlative stability are made possible by J-aggregates' greater red-shifted absorbance (100 nm) due to their aggregated orientation (Vincy et al., 2022) .

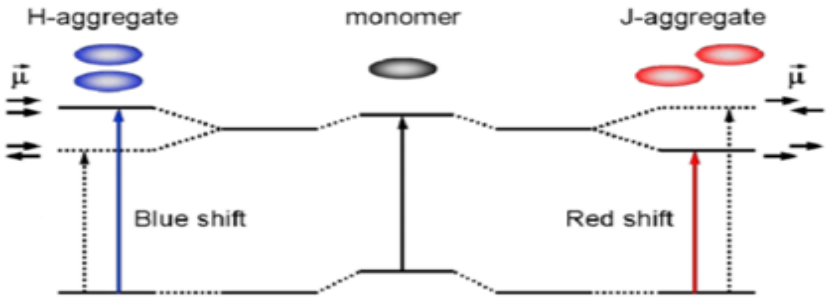

Figure 1.14. *Aggregation peaks in ICG* (Vincy et al., 2022)

Chapter 2

Review of past work and problem formulation

Cancer represents a significant global public health concern. On account of global demographic factors, the incidence of cancer is projected to rise over the coming decades, with more than 20 million new cases anticipated annually by 2025 (Zugazagoitia et al., 2016). Radiation therapy, chemotherapy, and surgical excision are the three primary methods employed in the treatment of cancer. However, there are certain limitations to conventional chemotherapy such as limited aqueous solubility of the majority of chemotherapeutics and lack selectivity toward cancerous cells. Furthermore, multidrug resistance (MDR): The primary cause of multidrug resistance (MDR) is the overexpression of efflux transporters in the cell membrane, such as P-glycoprotein (Pgp), which facilitate the exit of cells carrying a variety of anticancer drugs (Chidambaram et al., 2011). In clinical practice, the application of radiation doses is typically constrained by the imperative to minimize the occurrence and intensity of adverse effects. Late side effects, which are those that manifest or endure for a duration exceeding three months following the cessation of treatment, have a greater degree of "dose-limiting" significance than acute effects due to their potential for progressive severity and permanent nature (Dearnaley et al., 1999).Therefore conventional cancer treatments have several side effects hence in this scenario a new effective promising treatment will be beneficial.

Heat has emerged as a prominent technique in tumor therapy ever since its initial application in 1700 BC when a glowing fire drill point was employed to treat breast cancer. Subsequent advancements in heating technology, including ultrasound waves, radiofrequency, and microwaves sources, were implemented to stimulate moderate heating in a designated area, a process known as hyperthermia. The condition is frequently described as tissue being heated to a range of 41–47°C for several minutes (Huang et al., 2008). Photothermal therapy (PTT) is an

emerging and promising therapeutic approach that utilizes photo absorbers to produce thermal energy that induces the destruction of cancer cells when exposed to laser light. PTT demonstrates distinct advantages in cancer therapy when compared to conventional therapeutic modalities. These advantages encompass high specificity, minimal invasiveness, precise spatial-temporal selectivity, and more. To combat the initial stage of cancer metastasis, PTT can directly eliminate cancer cells in the primary tumor. Furthermore, it can be combined with existing therapeutic modalities to address cancer cells at metastatic sites (Zou et al., 2016). To enhance the efficacy and effectiveness of PTT researchers started to use NIR excitation to treat deeper tumors. The Near-Infrared (NIR) photothermal method is considered better than Ultraviolet-Visible (UV-Vis) photothermal for several reasons. NIR light has a deeper tissue penetration capability compared to UV-Vis light, making it more suitable for treating solid tumors due to its ability to penetrate tissues more effectively.

Numerous researchers have established that nanomaterials can augment PTT-based cancer therapy via a variety of mechanisms. Nanotherapeutics, as an emerging platform, possesses the capacity to transform the domain of drug delivery fundamentally. Proteins are capable of producing nanocarriers that are biocompatible, biodegradable, and readily metabolizable. Enzymes that are endogenously present in the human body are capable of degrading protein-based nanocarriers (Doughty et al., 2019).

Additionally, it has been discovered that protein nanoparticles elicit a minimal or nonexistent immune response. Additionally, proteins are capable of interacting with hydrophobic and hydrophilic solvents and medications due to their amphiphilic structure (Herrera Estrada & Champion, 2015). Therefore in this project, we have chosen silk fibroin nanoparticles which have several advantages enhanced biocompatibility, biodegradability, and negligible immunogenic response (Pham & Tiyaboonchai, 2020).

We Hei et.al’s study presents a novel method by merging silk fibroin nanofibers with a hydrogel to produce an injectable system. This hybrid material has a dual function: it enables the visualization of tumors by upconversion luminescence and also facilitates targeted photothermal therapy. The nanofibers, renowned for their biocompatibility, are incorporated into the hydrogel matrix, enabling seamless administration via direct injection into tumor locations. This technology demonstrates the capability to visualize tumors without the need for invasive procedures and generate heat in a specific area to eliminate cancer cells. It presents a viable approach for accurate and less intrusive cancer therapy. Nevertheless, additional investigation and experimentation, encompassing preclinical investigations and clinical trials, are imperative to validate its safety and effectiveness for practical medicinal use (He et al., 2019) .

According to De-Li ZhuGe et al ,"Cross-linked nanoparticles of silk fibroin with proanthocyanidins as a promising vehicle of indocyanine green for photo-thermal therapy of glioma". A novel strategy for treating glioma, a type of brain tumor, is being investigated through the utilization of proanthocyanidins and silk fibroin to generate nanoparticles capable of transporting indocyanine green to the site of the tumor. The research revealed that the nanoparticles exhibited efficacy in administering indocyanine green to the site of the tumor and stimulating photo-thermal therapy, thereby presenting a potential therapeutic avenue for glioma (Zou et al., 2016) . In this study, we have chosen ICG as our photothermal agent because it is an FDA-approved NIR chromophore. It has significant absorption and emission wavelength also it has an excellent safety profile.

ICG is desired in PTT due to its high photothermal conversion rate due to its low toxicity. So, ICG exhibits promise as a theranostic nanoplatform for cancer treatment (ZhuGe et al., 2019).

A comprehensive study on the development of a multifunctional scaffold for the treatment of bone tumors, specifically osteosarcoma,

was presented in Meng et al.'s preparation of polydopamine-modified silk fibrous/curcumin nanofibrous scaffolds for chemo photothermal therapy of bone tumors. Designed to facilitate chemo-photothermal therapy, the scaffold consists of silk fibroin, curcumin, and polydopamine. This presents a potentially effective strategy for optimizing treatment efficacy while reducing unfavorable consequences. Aspects of the scaffold that address the therapeutic and regenerative aspects of bone tumor treatment are highlighted in the research, including the controlled release of curcumin, its photothermal conversion efficiency of the ICG and DOX loaded silk fibroin nanoparticles for cancer research.

This thesis delves into an innovative strategy that combines photothermal and chemotherapy using nanotechnology, focusing on encapsulating Indocyanine Green (ICG) and Doxorubicin (DOX) within silk fibroin nanoparticles. This approach aims to significantly enhance the efficacy of cancer treatments. ICG, activated by near-infrared (NIR) light, generates localized heat, leading to hyperthermia in targeted tumor cells. This effect not only directly damages cancer cells but also improves the permeability of tumor vasculature, aiding in better drug delivery. Meanwhile, DOX, a potent chemotherapeutic agent, induces apoptosis in cancer cells by intercalating DNA. The encapsulation within silk fibroin nanoparticles offers several advantages. It enables controlled and sustained release of the therapeutic agents, ensuring prolonged exposure to the tumor site while minimizing systemic toxicity. The biocompatible nature of silk fibroin further enhances stability and reduces immunogenicity.

By synergizing the photothermal effects of ICG with the cytotoxicity of DOX, this strategy addresses the limitations of conventional treatments. It holds promise for more effective cancer therapy. This research contributes to advancing nanomedicine, paving the way for precise cancer treatments with improved therapeutic outcomes.

OBJECTIVES

1) Fabrication of silk nanoparticles (SNPs) for optimized loading of chemotherapeutic agent and photothermal agent
2) Physico-chemical characterization of SNPs
3) In vitro assessment of photothermal and chemotherapeutic potential of SNPs

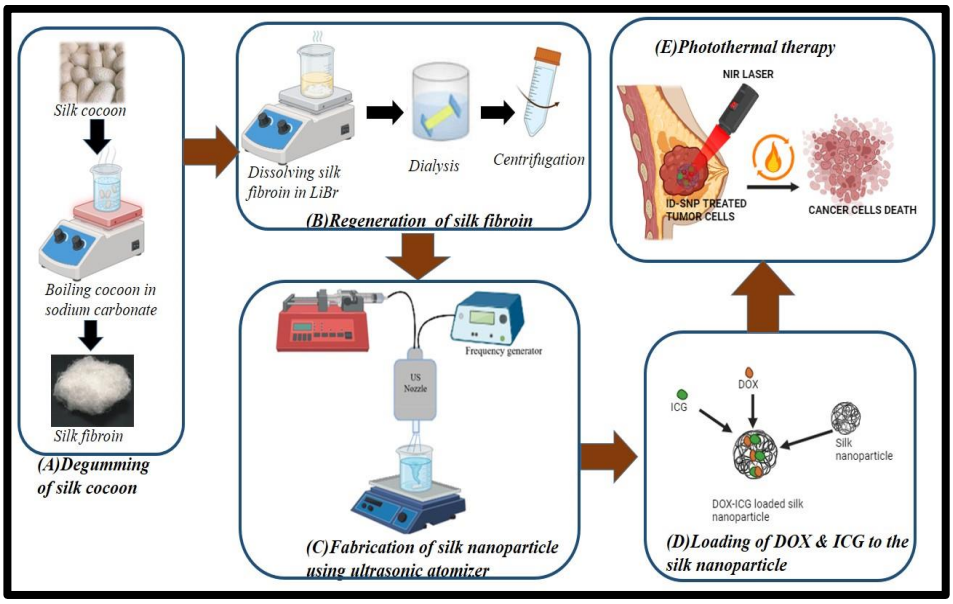

Figure 2. *The schematic illustration of silk nanoparticles for targeted combinational chemo and photothermal therapy.*

Chapter 3

Materials, method, and instrumentation

3.1 Materials. *Bombyx mori* cocoons were obtained from Krishi Vigyan Kendra, Agricultural Development Trust, Shardanagar Baramati, India. Snakeskin dialysis membrane (MWCO 3500) was purchased from Thermo Fisher Scientific Inc. Sodium carbonate anhydrous and acetone was purchased from Merck Emplura. Lithium bromide and Indocyanine green (ICG) were procured from Sigma Aldrich. Doxorubicin hydrochloride (DOX) was purchased from Tokyo Chemical Industry Co. Ltd. Ultrapure Milli Q was used to prepare all the samples. Gibco (Thermo Fisher Scientific Inc., India) supplied Dulbecco's modified Eagle's medium (DMEM, 1×), trypsin-EDTA (2.5%), and fetal bovine serum (FBS) for mammalian cell culture. We bought dimethyl sulfoxide (DMSO) from Merck (Germany). HiMedia (India) provided the 3-(4,5-dimethylthiazol-2-yl)-2,5-diphenyl tetrazolium bromide (MTT). Sigma provided us with the propidium iodide dye.

3.2 Instrumentation

3.2.1 UV-VIS Spectroscopy

UV-Vis spectroscopy is an analytical method that counts the number of distinct UV or visible light wavelengths that a sample absorbs or transmits through it in comparison to a reference or blank sample.This type of absorption happens when light energy is absorbed by the sample, raising the electrons' energy level.Due to the energy needed to excite electrons, different substances absorb light at different wavelengths, revealing details about the concentration and composition of the sample.The basis for absorbance spectroscopy is the Beer-Lambert law, which states that the absorbance (A) is proportional to the absorbing species' concentration (c), the sample's route length (l), and its molar absorptivity (ε).Quantitative and qualitative data regarding a molecule or substance can be obtained via UV-Vis spectroscopy (Perkampus, 2013).

3.2.2 Fluorimetry

The measurement of the fluorescence light released when a material absorbs light energy is known as fluorimetry.Fluorimetry is based on the phenomena of fluorescence, which is the instantaneous emission of visible light or radiation by specific compounds following their absorption of light energy.Fluorimetry can yield quantitative information by employing calibration curves to relate the fluorescence intensity to the fluorescent analyte's concentration, as well as qualitative information such determining the presence of specific fluorescent chemicals (Bigger et al., 1992).

3.2.3 Circular Dichroism

Circular dichroism (CD) spectroscopy is a method used to detect the difference in absorption between left-handed and right-handed circularly polarized light by chiral molecules.. This difference in absorption arises from the structural asymmetry of chiral molecules, which interact differently with the two forms of polarized light. CD spectroscopy is widely used to study the secondary structure of proteins, as well as the conformations of other biomolecules like peptides, lipids, RNA, and DNA (Perkampus, 2013).

3.2.4 TCS-PC

The principle of Time-Correlated Single Photon Counting (TCSPC) involves detecting single photons of a periodic light signal and determining the times of these photons after the excitation pulse. TCSPC is a technique that records the time between an excitation pulse and the detection of a single emitted photon.A pulsed light source, such as a laser, is used to excite the sample, and a detector converts the emitted photons into electronic pulses.The TCSPC electronics precisely measure the arrival time of each detected photon relative to the excitation pulse.Many thousands of these arrival times are recorded and sorted into a histogram, which represents the statistical distribution of photon emission over time after excitation.TCSPC has high time resolution, photon efficiency, dynamic range, and linearity, making it

well-suited for measuring fluorescence lifetimes.Limitations include a maximum count rate related to the detector dead time, where only one photon per excitation pulse can typically be detected. In TCSPC (Time-Correlated Single Photon Counting), the pulse repetition rate of the signal is significantly higher than the photon detection rate, making it highly unlikely to detect multiple photons within a single signal period.This technique achieves near-ideal photon efficiency, high time resolution, and an extremely high dynamic range and linearity. TCSPC builds up a distribution of photons over time after excitation, representing the waveform of the optical signal with exceptional precision and efficiency (Perkampus, 2013).

3.2.5 Fluorescence microscopy

The principle of fluorescence microscopy is that fluorescent molecules or fluorophores within a sample are excited by a specific wavelength of light, causing them to emit light at a longer wavelength.The emitted fluorescent light is then detected and used to create an image of the sample. Fluorescence microscopy allows for high-contrast imaging of specific structures or molecules that have been labeled with fluorescent dyes or proteins. It is a powerful technique for visualizing subcellular structures and dynamics in biological samples.Key components of a fluorescence microscope include a light source, excitation and emission filters, and a dichroic mirror to separate excitation and emission wavelengths. Various fluorescent dyes and stains are used in fluorescence microscopy to label specific cellular components or structures for visualization.Examples of fluorescent dyes include nucleic acid stains like Hoechst and DAPI for labeling the nucleus, phalloidin for staining actin fibers, and fluorochromes like Alexa Fluor for specific targets. Fluorescence microscopy is essential in cell biology, molecular biology, and biotechnology, enabling the tracing of molecules in live cells and the study of cell metabolism, mutation, and toxicity.The technique allows for high-contrast imaging of specific structures within cells and tissues, making it a valuable tool for biological research (Perkampus, 2013).

3.3 Methods

3.3.1 Silk nanoparticle fabrication: *Bombyx mori* cocoons were subjected to a sequential process involving chopping and boiling in 0.005M sodium carbonate solution to eliminate sericin and extract silk fibroin. The resultant fibroin was washed with ultrapure Milli Q water and dried at 37°C. Manual disentanglement preceded dissolution in lithium bromide at 60°C for 4-6 hours. The silk fibroin solution was dialyzed against ultrapure Milli Q water for 48 hours, undergoing two sets of centrifugations at 12700 rpm for 30 mins. The supernatant obtained constituted the regenerated silk fibroin solution. Silk nanoparticles (SNPs) were prepared by forming a 0.7% w/v silk fibroin solution in Milli Q water, followed by ultrasonic atomization at a frequency of 130 kHz and a sample flow rate of 0.2 mL/min. The regenerated silk fibroin solution, loaded in a syringe, was passed through sterile tubing and collected in a solvent mixture of acetone (45ml) and 0.2% PEG (5ml) set at 1500 rpm for homogenous mixing. After atomization, the nanoparticle solution underwent differential centrifugation to isolate the finest particles. The differential centrifugation of the sample was performed five times constituting 4800 rpm for 30min, 7800 rpm for 30 min, 10,000 rpm for 45min, 14,000 for 1hr, and 14,000 rpm for 3hrs, and every time the supernatant was centrifuged to get the smallest particle. The resulting pellet was re-suspended in Milli Q water, and subjected to sonication for 15-20 minutes, yielding a stock solution of silk nanoparticles (SNP). This method provides a systematic approach to the fabrication of silk nanoparticles with potential applications in various fields.

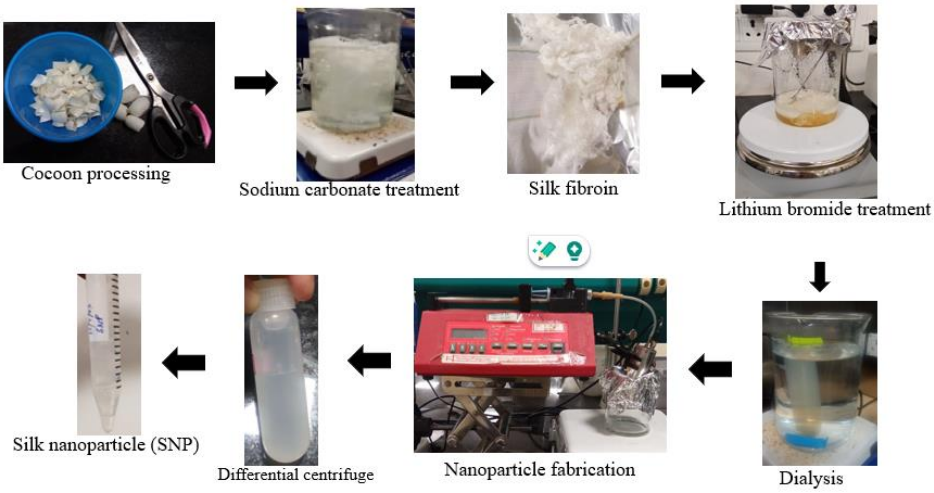

Figure 3.1 *Fabrication of silk nanoparticles.*

3.3.2 Loading of ICG and DOX into SNPs. Silk nanoparticles (SNPs) were loaded with indocyanine green (ICG) and further co-loaded with doxorubicin (DOX) to create a multifunctional theranostic platform. For ICG-loaded SNPs, 200 µL of SNPs were combined with 31 µL of ICG (stock concentration =0.5 mg/ml), and the total volume was adjusted to 1 mL using Milli Q water. In the case of ICG and DOX-loaded SNPs, 200 µL of SNPs were mixed with 31 µL of ICG (stock concentration =0.5 mg/ml) and 34 µL of DOX (stock concentration =1mg/ml), with the final volume adjusted to 1 mL using Milli Q water. The final concentration for DOX and ICG for loading is 60 µM and 20 µM. Subsequently, the samples were subjected to overnight incubation in a ROTOSPIN apparatus, followed by centrifugation at 14000 rpm for 3 hours. The resulting pellet was resuspended in MilliQ water and stored at 4°C, while the supernatant was also retained.

3.3.3 Encapsulation efficiency measurements. In this study, standard calibration curves were established to quantify the concentrations of Indocyanine Green (ICG) and Doxorubicin (DOX) in silk nanoparticle formulations. For the ICG calibration curve, various concentrations ranging from 0 to 25 µM were prepared, and the corresponding absorbance at 780 nm was recorded. Similarly, the DOX calibration curve was generated by preparing diverse concentrations spanning from 5 to 100 µM, with absorbance measurements taken at 480 nm. The

absorbance spectra of the silk nanoparticle pellet and supernatant were acquired across the wavelength range of 350 nm to 900 nm. Subsequently, the concentrations of ICG and DOX in both the pellet and supernatant were determined utilizing the respective calibration curves. This comprehensive approach enables precise quantification of encapsulated ICG and DOX within silk nanoparticles, thereby facilitating the characterization of drug loading efficiency and distribution in the nanoparticle formulation**.** Then the encapsulation efficiency was calculated with the following equation:

$$EE(ICG\ or\ DOX)\% = \left(1 - \frac{[concentration\ of\ ICG\ or\ DOX\ left\ in\ supernatant]}{[total\ concentration\ ICG\ or\ DOX\ used\ for\ encapsulation]}\right) x\ 100\%$$

3.3.4 Fluorescence measurements: Emission spectra of the samples (ICG loaded silk nanoparticles pellet and supernatant; ICG and DOX loaded silk nanoparticles) were taken with excitation at 680nm and emission at 700-900nm with the Fluorolog-3 spectrofluorometer.

3.3.5 CD spectra: The ICG-loaded silk nanoparticles (ISNP) and ICG and DOX-loaded silk nanoparticles pellet (IDSNP) were resuspended in Milli-Q and then different dilutions were prepared for CD spectra. The bare silk nanoparticles were also diluted. Then the program for the spectra was set at 170- 290nm and scan speed at 50nm/sec for all the samples.

3.3.6 Time-resolved fluorescence measurements: A picosecond TCSPC (time-correlated single-photon counting) device from Horiba (Fluorocube-01-NL) was used to measure the lifetimes of free ICG, ICG-loaded silk nanoparticles, and ICG and DOX-loaded silk nanoparticles. Using a picosecond diode laser, the samples were stimulated at 405 nm, and the decays were recorded at an emission wavelength of 550 nm. To get rid of the scattered light, we employed a filter on the emission side. The signals were obtained using a photomultiplier tube (TBX-07C) detector with an instrument response function of about 140 ps for the 405 nm laser, with magic-angle (54.75°) polarization. The IBH DAS version 6 decay analysis program was used to analyze the data. We kept the temperature (T) constant at 25 °C during

every experiment. We fitted a multiexponential function to the decays according to the equation:

$$D\ (t) = \sum_{i=1}^{n} a_i \exp(\frac{-t}{\tau_i})$$

where a_i is the normalized amplitude of the decay components τ_i and D(t) is the normalized fluorescence decay. Reduced chi-square ($\chi 2$) values and the corresponding residual distribution were used to assess the fit quality. The $\chi 2$ of the acceptable fit is almost unity.

3.3.7 SEM imaging: The morphological analysis of the synthesized silk nanoparticles was conducted utilizing a field-emission scanning electron microscope (FE-SEM). Glass slides were meticulously prepared by sectioning into smaller dimensions using a diamond cutter and subsequently cleansed with alcohol. The nanoparticle samples were prepared through an initial step of sonication lasting 10-15 minutes, followed by the careful drop-casting of a minute quantity of the specimen onto the glass slides. The prepared samples were then left in a desiccator overnight for drying. Subsequently, the glass slide samples were affixed onto a stub using carbon tape. To enhance conductivity, a 10 nm layer of gold was sputtered onto the nanoparticles for 2 minutes. The modified samples were subjected to analysis using a 5-10 kV electron beam in the FE-SEM instrument. Then the size distribution of the nanoparticles was measured using Image J software.

3.3.8 Photothermal assessment of ICG and DOX-loaded SNPs. To assess the photothermal capability of IDSNPs 808 nm laser was used. Firstly, to prepare ICG and DOX-loaded SNPs, 200 µL of SNPs were mixed with 31 µL of ICG (0.5% stock solution) and 34 µL of DOX (1.0% stock solution), with the final volume adjusted to 1 mL using Milli Q water. Subsequently, the samples were subjected to overnight incubation in a ROTOSPIN apparatus, followed by centrifugation at 14000 rpm for 3 hours. The resulting pellet was resuspended in Milli Q water and the supernatant was discarded. Then a particular dilution of

IDSNP was irradiated with an 808 nm laser at 0.66 W, 0.88 W, and 1.09 W, and at different time points (30s-180s) the temperature change was observed. The concentration-dependent photothermal assay was performed by preparing three dilutions 10 µM, 15 µM, and 20 µM and then irradiating these samples with 808 nm laser at 0.66 W and at different time points (30s-180s) the temperature change was observed.

IDSNPs were irradiated with an 808 nm laser for 3min at 0.66 W and then a thermal image was taken with Fluke Infrared Thermal Imaging Camera at the 30s, 60s, 90s,120s,180s, and 180s. The thermal image was taken with the help of Fluke Connect software to analyze the maximum temperature.

Photothermal stability of free ICG and IDSNPs was investigated by laser on/off cycles. The free ICG and IDSNP solutions were prepared and irradiated with 808 nm at 0.66 W laser for 5 minutes and then cooled for 10 minutes this way four cycles of laser-on/off were performed and temperature was recorded every 2min.

3.3.9 Cellular viability of ICG and DOX-loaded SNPs.

MTT assay was performed to examine the cellular viability of free DOX and IDSNPs on HeLa cells. To perform this experiment 5000 cells/well were counted on a hemocytometer and then seeded in 96 well plate and kept in CO_2 incubator overnight. The next day the cells were observed under the microscope to confirm the confluency and then it was treated with different dilutions of free DOX and IDSNPs.The different dilutions for free DOX were prepared as such 5 µM,10 µM, 15 µM, 20 µM, 30 µM,40 µM,50 µM, and 60 µM. The different dilutions for IDSNPs were prepared as such 4 µM,8 µM, 10 µM, 12 µM, 16 µM, and 20 µM. Then after treating the cells with free DOX and IDSNPs it was incubated for 24hrs and then the media containing free DOX and IDSNPs were removed and 100 µL of MTT (Stock concentration 5mg/ml and working concentration 0.5mg/ml) was added and incubated for 4hrs and then the media containing MTT was aspirated off and 100 µL DMSO was added to each well and incubated for 20-30 mins and absorbance was recorded

at 570 nm in UV–vis microplate reader (Synergy H1). The control for this experiment was untreated cells and the MTT assay was performed in triplicates for each dilution. Then the IC50 for free DOX and IDSNPs were calculated using GraphPad Prism 8 software.

MTT assay was performed to examine the cellular viability of laser-untreated IDSNPs and laser-treated IDSNPs on HeLa cells. To perform this experiment 5000 cells/well were counted on a hemocytometer and then seeded in 96 well plate and kept in CO_2 incubator overnight. The next day the cells were observed under the microscope to confirm the confluency and then it was treated with different dilutions of IDSNPs. The different dilutions for IDSNPs were prepared as such 4 µM,8 µM, 10 µM, 12 µM, 16 µM, and 20 µM. Then after treating the cells with IDSNPs, it was incubated for 6hrs and then each well was irradiated with 808nm laser at 1.09 W for 3 min but the control wells containing IDSNPs treated cells were not irradiated. Then the media containing IDSNPs were removed and 100 µL of MTT (Stock concentration=5 mg/ml and working concentration= 0.5 mg/ml) was added and incubated for 4hrs and then the media containing MTT was aspirated off and 100 µL DMSO was added to each well and incubated for 20-30 mins and absorbance was recorded at 570 nm in UV–vis microplate reader (Synergy H1).The control for this experiment was untreated cells and the MTT assay was performed in triplicates for each dilution.

3.3.10 Cellular uptake of ICG and DOX-loaded SNPs.

HeLa cells were seeded at a density of 0.05×10^6 cells/well on a 24-well plate for cellular uptake. The next day the cells were treated with ID-SNPs and incubated for 6 hours. Cells that had not been treated were served as the negative control. Following the treatment, the cells were subjected to a 1× PBS wash, fixed with 4% paraformaldehyde, and examined using a Nikon Eclipse Ti-U fluorescent microscope that had a mercury lamp and a camera for capturing images. The fluorescence images were captured in the green channel for DOX and NIR filter for ICG.

3.3.11 PI Staining of ICG and DOX-loaded SNPs.

Propidium Iodide (PI) staining was performed to observe the cell death due to the treatment of IDSNPs. To perform this experiment 5000 cells/well were counted on a hemocytometer and then seeded in 96 well plate and kept in CO_2 incubator overnight. The next day the cells were observed under the microscope to confirm the confluency and then it was treated with IDSNPs. Then after treating the cells with IDSNPs, it was incubated for 6hrs and then each well was irradiated with 808nm laser at 1.09 W for 3 min but the control wells containing IDSNPs treated cells were not irradiated. Then the media containing IDSNPs was removed and 40 µL of 1µg/ml PI (Stock concentration =10mg/ml; the PI solution was prepared in 1xPBS) was added and then incubated for 15 mins after that the PI solution was removed and then observed under Nikon Eclipse Ti-U fluorescent microscope. The fluorescence images were captured in the red channel.

Chapter 4

Results and observations

We have fabricated DOX and ICG-loaded silk nanoparticles (IDSNPs). Their characterization was done to confirm the loading of molecules and the size of the nanoparticles.

4.1. Absorption and Fluorescence Spectra. The ICG-loaded silk nanoparticles (ISNP) and ICG and DOX loaded silk nanoparticles (IDSNP) were prepared. To confirm the loading of ICG and DOX in the silk nanoparticles the absorption and emission spectra were obtained. Figure 4.1.A represents the absorption spectra of the ICG-loaded silk nanoparticles (ISNP) pellet and supernatant. The spectra show two characteristic absorption bands of ICG at ~720 nm and ~780 nm. In this curve, the black line represents the absorption spectrum of the ISNP's pellet which is much lower as compared to the absorption spectrum of the supernatant as shown in the red line. This suggests that in the case of ISNPs majority of ICG is left in the supernatant in comparison with the pellet. This signifies that ISNP has a low encapsulation efficiency for ICG.

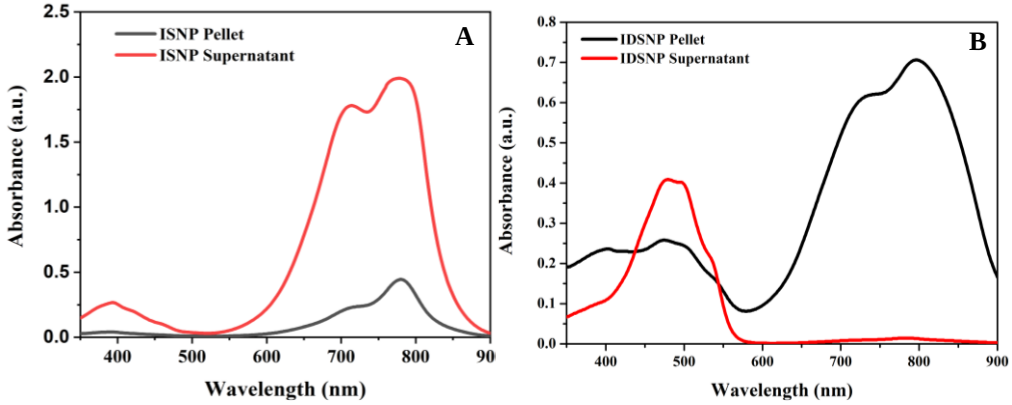

Figure 4.1. (A) *Absorption spectra of ICG-loaded silk nanoparticles at 350-900 nm where the black line represents the absorption spectrum of the pellet and the red line represents the absorption spectrum of the supernatant* ***(B)*** *Absorption spectra of ICG and DOX loaded silk nanoparticles at 350-900 nm where the black line shows the absorption spectrum of the pellet and red line represents absorption spectrum of the supernatant.*

Figure 4.1.B represents the absorption spectra of the pellet and supernatant of ICG and DOX-loaded silk nanoparticles. The absorption spectrum of IDSNPs pellet shows two characteristic peaks of ICG at ~725 nm and ~800 nm and one band at ~480 due to DOX. The absorption spectrum of supernatant shows an absorption band due to DOX at ~480 nm and negligible absorption in the NIR wavelength range. These findings suggest that in the presence of DOX majority of ICG gets encapsulated within silk nanoparticles. Therefore, it can be concluded that DOX plays a significant role in improving the loading efficiency of ICG within silk nanoparticles. Then to accurately calculate the encapsulation efficiency of ICG and DOX the calibration curves for free ICG and free DOX were used. Figure 4.2.A. and Figure 4.2.B show the calibration curves of free ICG and DOX respectively. The encapsulation efficiency of ICG for ISNP and IDSNP was found to be ~20% and ~98% of ICG respectively. The encapsulation efficiency of DOX was calculated using the DOX calibration curve and it was found to be ~35%.

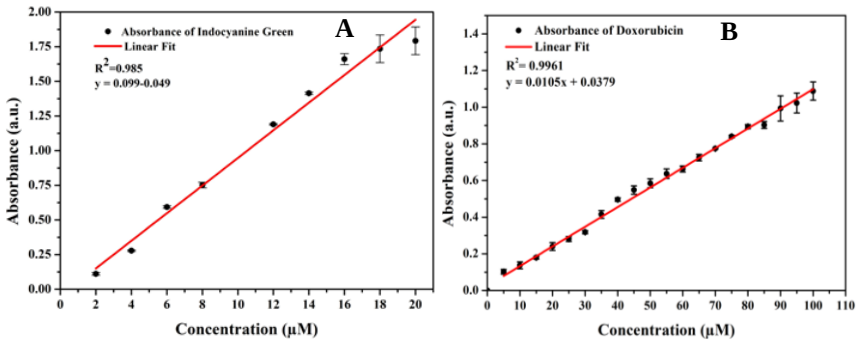

Figure 4.2. (A) *Calibration curve for Indocyanine green (ICG).* ***(B)*** *Calibration curve for Doxorubicin (DOX).*

To further assess the role of DOX in the loading efficiency of ICG within the silk nanoparticles, the absorption spectra of free ICG and IDSNP were compared as represented in Figure 4.3.A. To understand peak broadening quantitively the absorption curve was fitted to the Gaussian curves as shown in Figure 4.3.B. Hence, upon Gaussian peak fitting we observed 3 peaks – Peak 1 at ~725 nm corresponds to the H band due to the H aggregation, Peak 2 at ~800 nm corresponds to M the

monomeric peak but there is a shift in the peak position of the monomeric peak and the Peak 3 at ~851 nm corresponds to the J Band due to the J aggregation. The Gaussian peak fitting revealed the presence of the additional peak at ~851 nm. This peak confirms the presence of J aggregation of ICG in IDSNPs. Therefore, from here we conclude that DOX plays a significant role in the loading efficiency of ICG and the formation of J aggregates of ICG.

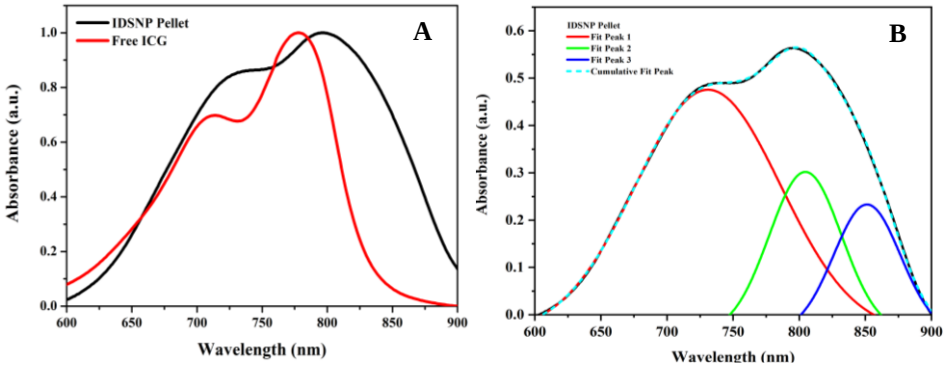

Figure 4.3.(A) *Absorption spectra of free ICG and IDSNP which confirms the broadening of curve.* ***(B)*** *Gaussian peak fitting of Absorption spectra of ICG and DOX loaded silk nanoparticles where peak 1 denotes ICG H aggregation (~725 nm), peak 2 denotes ICG monomeric peak (~800 nm) and peak 3 denotes ICG J aggregation peak (~851nm).*

To further confirm the encapsulation of ICG the emission spectra were observed in the NIR wavelength range since ICG is a fluorescent NIR chromophore. Figure 4.4.A represents the emission spectra of ICG-loaded silk nanoparticles. The spectra show a characteristic fluorescence peak of ICG at ~810nm. It was observed that the emission spectrum of the supernatant is much higher than the fluorescence spectrum of the pellet which signifies the large amount of ICG in the supernatant. Figure 4.4.B represents the emission spectra of ICG and DOX-loaded silk nanoparticles. The spectra show a characteristic peak of ICG at ~810nm. The emission spectrum of the IDSNP pellet is much higher than the supernatant which signifies the large amount of ICG in the pellet and

better encapsulation. Therefore, from the emission spectra also we can deduce that the encapsulation efficiency is higher for IDSNP as compared to ISNP.

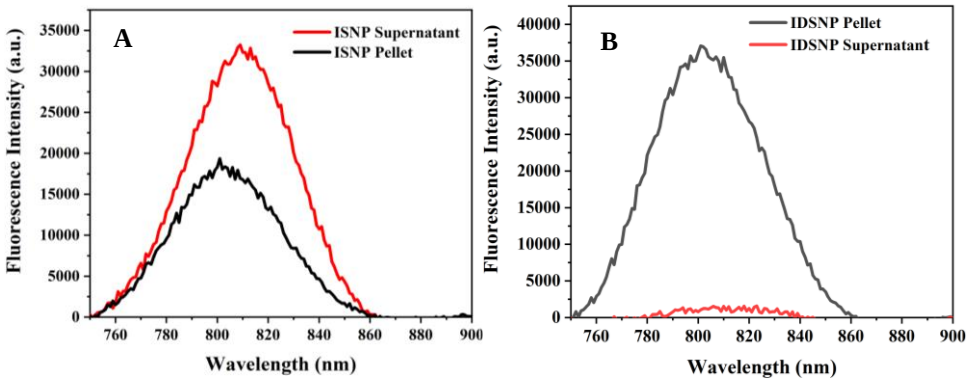

Figure 4.4. (A) *Fluorescence spectra of ICG-loaded silk nanoparticles with excitation at 680 nm and emission at 700-900 nm where the black line represents the pellet and the red line represents the supernatant.* ***(B)****Fluorescence spectra of ICG and DOX loaded silk nanoparticles with excitation at 680 nm and emission at 700-900 nm where the black line represents the pellet and the red line represents the supernatant.*

4.2. CD Spectra analysis. To evaluate potential conformational changes in the protein component of our nanoparticles after loading with DOX and ICG, we analysed the Circular Dichroism (CD) spectra. Figure 4.5. shows CD spectra of bare silk nanoparticles, ICG-loaded silk nanoparticles, and ICG and DOX loaded silk nanoparticles. It has been observed that the bare SNP has a defined beta sheet according to the CD spectra. This might be due to the exposure of the nanoparticles to acetone(Jaiswal et al., 2022). In the case of ISNP and IDSNP, there is a change in the peak position which could be a change in the beta-sheet structure and this might be due to the interaction of the ICG and DOX with the silk nanoparticles. Hence, we can conclude that interactions of silk nanoparticles with ICG and DOX might be inducing secondary structural changes.

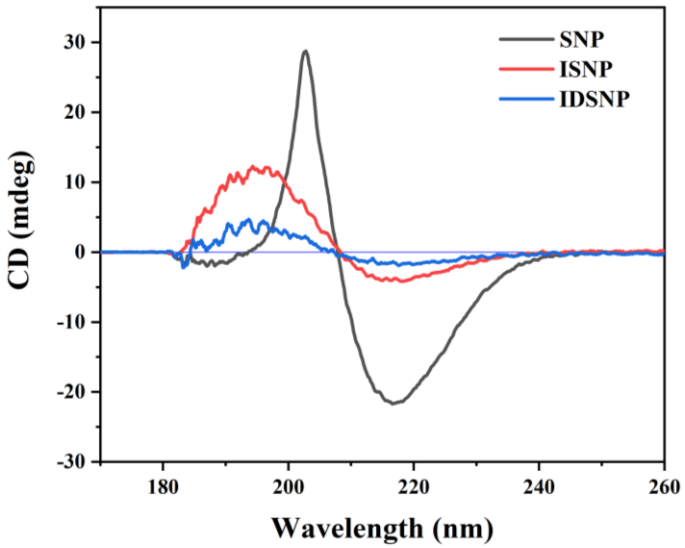

Figure 4.5 *CD spectra of bare silk nanoparticles, ICG-loaded silk nanoparticles, and ICG and DOX-loaded silk nanoparticles.*

4.3. Fluorescence lifetime estimation. The fluorescence lifetime helps us to determine the stability of the fluorescent molecules. Therefore, to check whether the interaction of the DOX and ICG with the silk nanoparticles affects the stability of ICG the fluorescence lifetime measurement was done. Figure 4.6.A shows that after exciting the samples at 405 nm free ICG decays faster than the ICG-loaded silk nanoparticles. We also observed from Table 4.1. that the average lifetime of free ICG (1.179) is less than the ISNP (2.467). Therefore, we conclude that ICG is getting more stable in the nano-encapsulated form. In the case of ICG and DOX-loaded silk nanoparticles (IDSNP), in Figure 4.6.B**,** a sharp decline in the decay curve is noticed due to the absorption region of DOX around 450-550nm. We also observed from Table 4.1. that the average lifetime of IDSNP (1.008) is less than the ISNP (2.467). Since lifetime decreases, most of the absorption is utilized in the non-radiative relaxation process. Therefore, most of the energy is utilized in elevating the temperature. So, IDSNPs might be suitable for producing heat upon laser exposure.

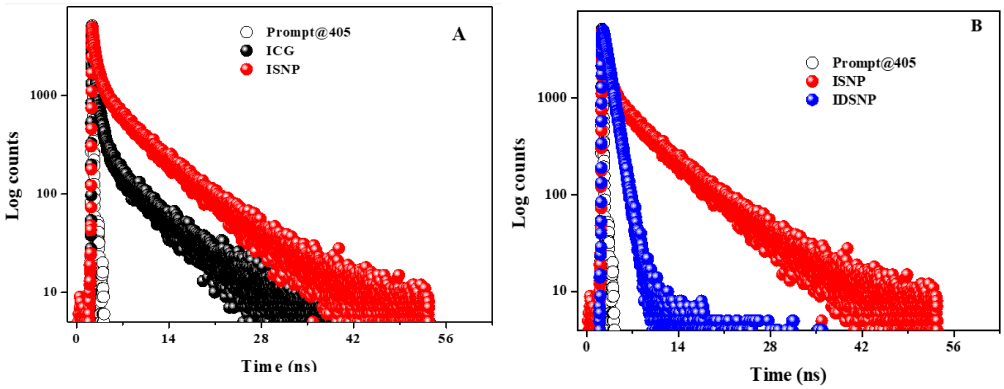

Figure 4.6.(A) *Fluorescence lifetime decay curve of free ICG and ICG loaded silk nanoparticle where excitation wavelength is 405 nm and emission wavelength is 550 nm.* ***(B)*** *Fluorescence lifetime decay curve of ICG loaded silk nanoparticle and ICG and DOX loaded silk nanoparticle where excitation wavelength is 405 nm and the emission wavelength is 550 nm.*

Table 4.1 *Time-resolved fluorescence lifetime estimation.*

Sample	χ^2	**a1**	T1 ns	**a2**	**T2 ns**	**<T> ns**
ICG	1.15	0.043	0.629	0.0047	6.215	1.179
ISNP	1.16	0.046	0.786	0.0179	6.793	2.467
IDSNP	1.08	0.079	0.948	0.026	1.193	1.008

4.4. SEM imaging. The morphological characterization of silk nanoparticles (SNPs) was conducted utilizing field emission scanning electron microscopy (FE-SEM). FE-SEM imaging facilitated the examination of the morphology of silk nanoparticles. Figure 4.7 shows the SEM images of bare SNPs. FE-SEM analysis confirmed the average size of the SNPs to be approximately ~70 ± 4 nm. Figure 4.8 shows the

SEM images of ICG and DOX-loaded SNPs. FE-SEM analysis confirmed the average size of the IDSNPs to be approximately 80 ± 4 nm. Therefore, the increase in the nanoparticle size might be due to the loading of ICG and DOX in the silk nanoparticles.

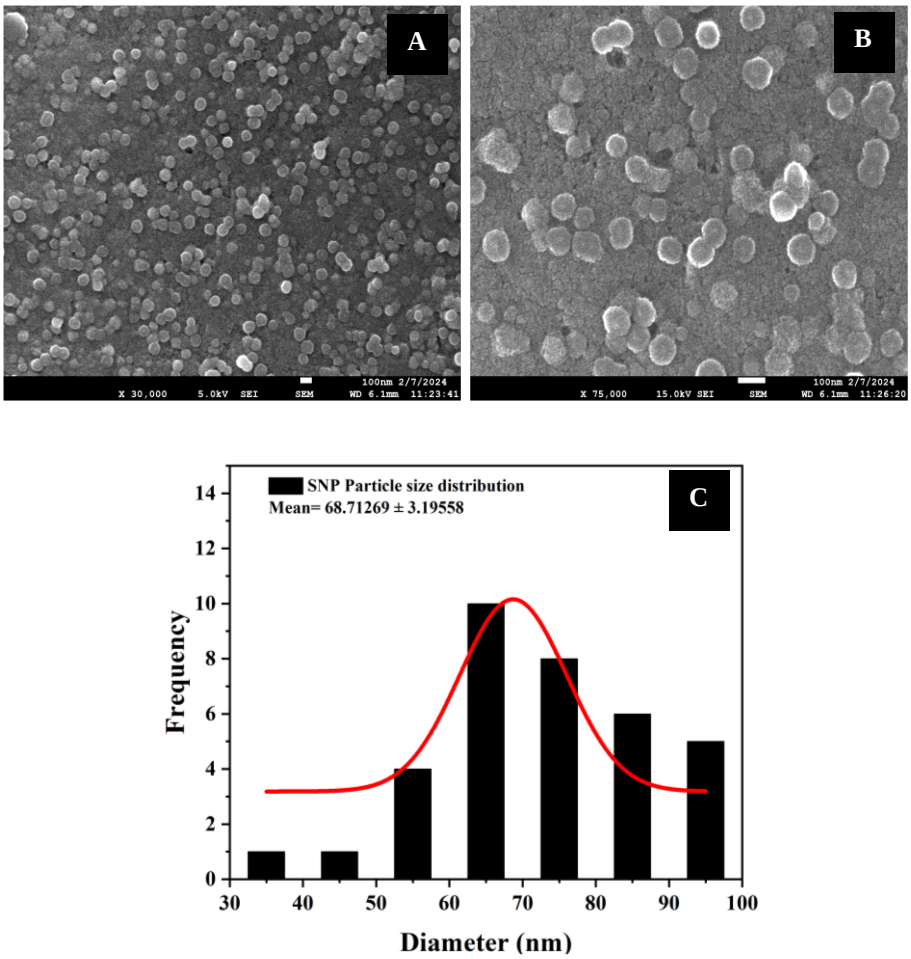

Figure 4.7. (A) *SEM image of bare silk nanoparticles at 30,000 x* ***(B)*** *SEM image of bare silk nanoparticles at 75,000 x.* ***(C)*** *Size distribution of bare nanoparticles.*

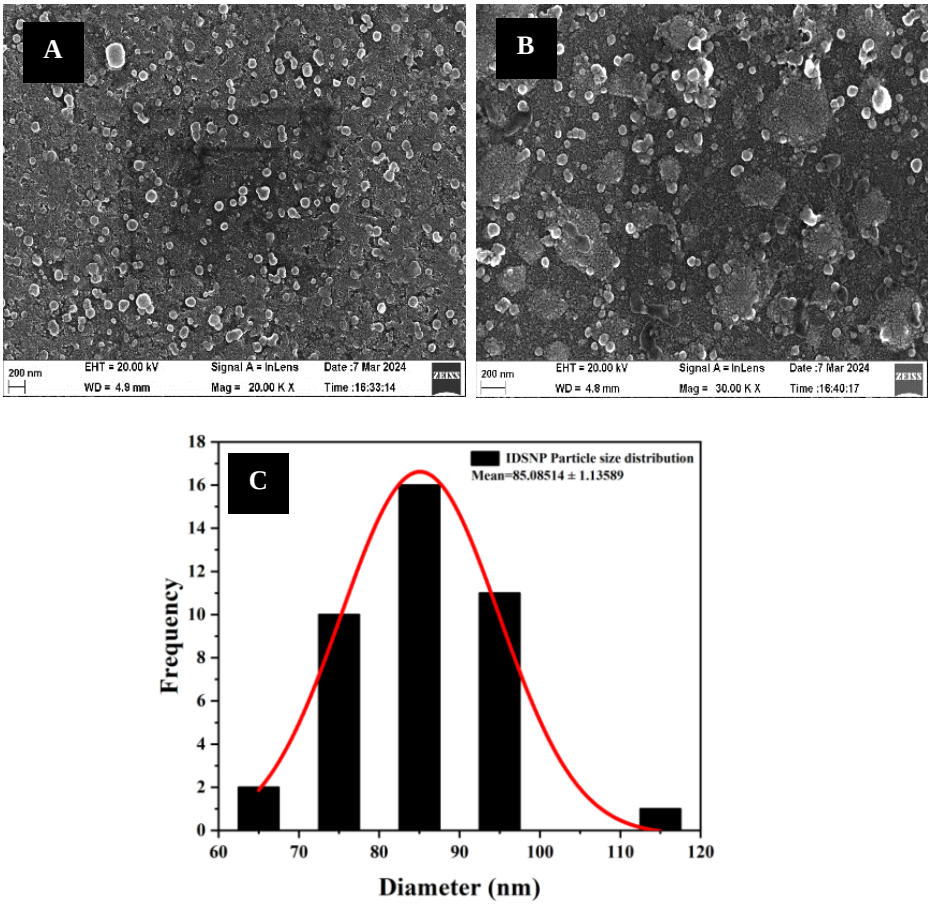

Figure 4.8. (A) *SEM image of ICG and DOX loaded silk nanoparticles at 20,000 x* ***(B)*** *SEM image of ICG and DOX loaded silk nanoparticles at 30,000 x.* ***(C)*** *Size distribution of ICG and DOX loaded silk nanoparticles.*

4.5. Photothermal assessment of ICG and DOX-loaded SNPs.The photothermal efficacy of the ICG and DOX loaded nanoparticles was assessed by irradiating the samples with an 808 nm laser. Figure 4.9.A. shows the temperature profile of IDSNPs upon irradiating with an 808nm laser at various power. When the samples were irradiated with three different powers (0.66 W, 0.88 W, and 1.09 W), the temperature was saturated at some point in all cases but the more the laser power, the faster the temperature increase was observed since more energy was provided for the excitation of the particles. In the case of 0.66 W the highest temperature that could be reached is 37°C, for 0.88 W it is 38°C

and for 1.09 W it is 39°C from room temperature. Figure 4.9.B shows the temperature profile of the three concentrations of IDSNPs exposed to the fixed laser power.When we are irradiating three different samples (10 µM, 15 µM, and 20 µM) with the same power, the temperature increases faster with increasing concentration since the amount of molecules getting excited. In the case of 10 µM the temperature change could be reached to 37°C, for 15 µM it is 38°C and for 20 µM it is 39°C. When the laser power density is increased, more energy is absorbed by the ICG, leading to a correspondingly larger amount of heat generated. Consequently, the temperature rises proportionally to the laser power density and the concentration of ICG in the solution. When the concentration increases then the number of particles increases resulting in higher frequency of collisions among the particles.

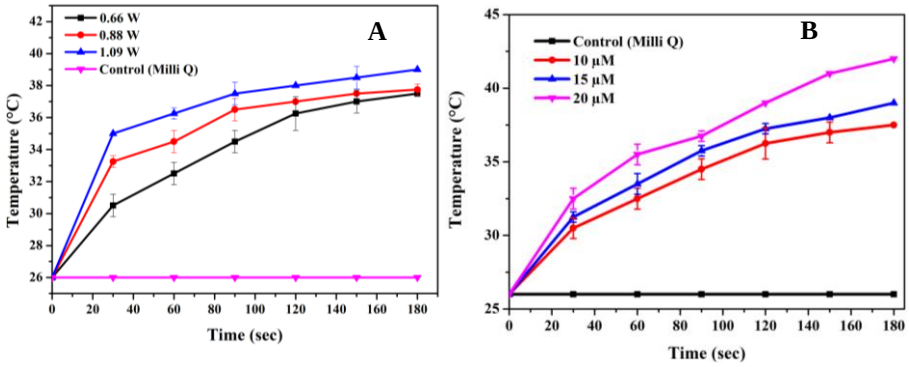

Figure 4.9 *Photothermal assessment of DOX and ICG loaded silk nanoparticles.* ***(A)*** *Temperature profile of 10 µM IDSNPs irradiated with 808nm laser at 0.66 W, 0.88 W, and 1.09 W.* ***(B)*** *Temperature profile of 3 different concentrations IDSNPs irradiated with 808nm laser at 0.66 W.*

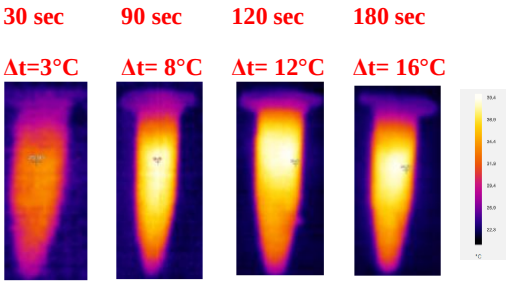

Figure 4.10 *IR Image of IDSNPs irradiated with 808 nm laser for 3min at 0.66 W.*

Figure 4.10 represents the thermal images of IDSNPs after irradiating with an 808 nm laser at 0.66 W where we can observe that the whitish-yellow region increases with increasing time since the temperature is increasing.

Figure 4.11 represents the photothermal stability of free ICG and IDSNPs after irradiating with an 808 nm laser at 0.66 W. In the case of IDSNPs when the laser is on for 5 minutes the temperature increased gradually and when the laser is off the temperature decreases gradually. This sample was again irradiated for 5 minutes and the temperature increased gradually this pattern was repeated several times confirming the photothermal stability of the ICG and DOX loaded silk nanoparticles. The increase in change in temperature was around 15°C when the laser was on and this change of temperature was almost maintained in subsequent cycles of laser on and off. In the case of free ICG when the laser is on for 5 minutes the temperature increased gradually but not as IDSNPs and when the laser is off the temperature decreases gradually. Free ICG was also exposed to laser three times but its temperature couldn't increase that much as compared to IDSNPs. This suggests that nano-encapsulated ICG is more stable in comparison with free ICG.

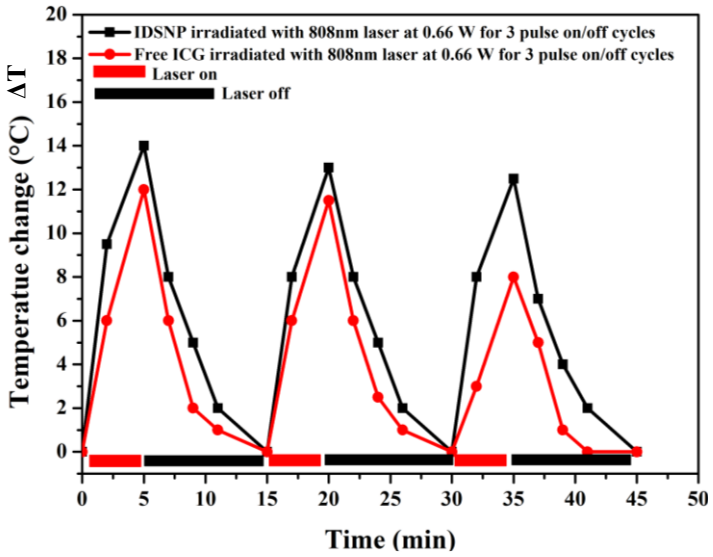

Figure 4.11 *Photothermal stability of free ICG and IDSNP in three on and off cycles*

4.7. Cellular viability of ICG and DOX-loaded SNPs. The *in-vitro* biocompatibility of ID-SNPs was evaluated with consideration of their potential biomedical applications. Figure 4.12 represents the cellular cytotoxicity of IDSNPs on HeLa cells over 24 hours. The IC50 value for free DOX is ~1.15 ± 0.02 µM which is less as compared to IDSNPs whose IC50 is ~0.6725 ± 0.02 µM. Therefore, IDSNPs are very effective in killing cancerous cells with less concentration than free DOX within 24 hours. Therefore, IDSNPs could be used as a promising therapeutic candidate to deliver DOX.

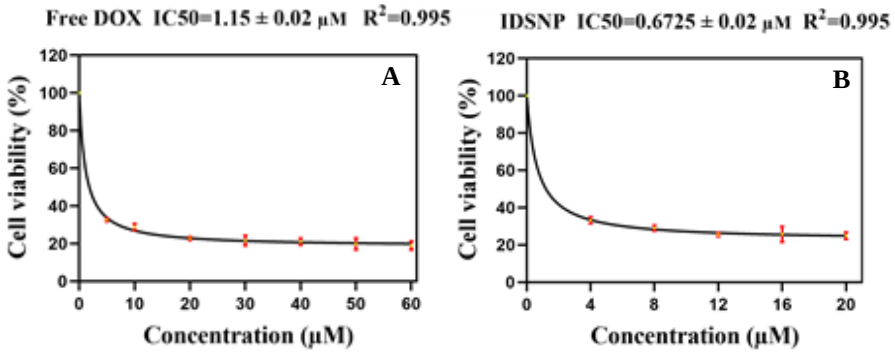

Figure 4.12 *Cellular viability analysis of free DOX and IDSNPs.*

Figure 4.13 illustrates the cellular viability of IDSNP-treated cells over 6 hours, comparing untreated cells (black bars) with cells subjected to a single laser exposure (red bars) at 1.09 W for 3 minutes. In the absence of laser treatment, IDSNP-treated cells exhibited varying degrees of cellular viability: 80% and 79% at lower concentrations (4 µM and 8 µM), and 75% and 65% at higher concentrations (16 µM and 20 µM). Conversely, upon laser exposure, the cellular viability decreased significantly, with viabilities of 78% and 70% at lower concentrations, and 34% and 32% at higher concentrations, respectively. This observed reduction in cellular viability underscores the potent cytotoxic effect of IDSNPs when combined with laser irradiation. Notably, this pronounced effect was evident within 6 hours of incubation with IDSNPs, highlighting their rapid and impactful action. Consequently, our findings underscore the dual functionality of IDSNPs as effective chemotherapeutic and photothermal agents, emphasizing the synergistic benefits derived from their combined therapeutic modalities. This

integrated approach holds considerable promise for enhancing cancer treatment outcomes by harnessing the synergistic potential of chemotherapeutic and photothermal therapies.

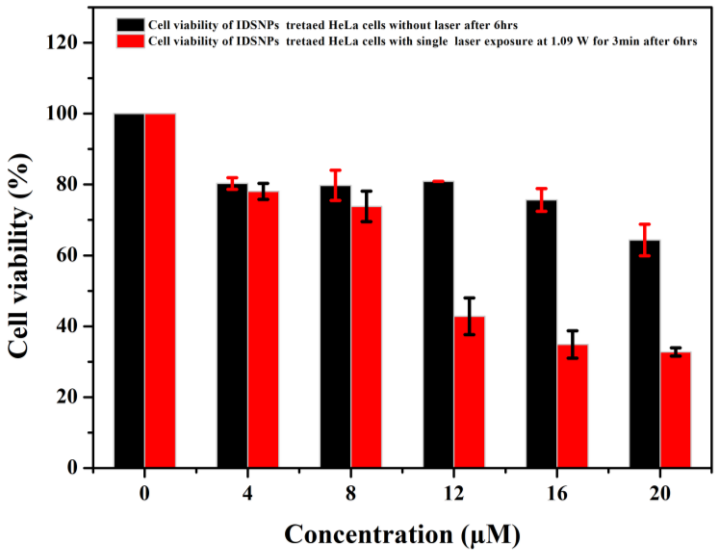

Figure 4.13 *Cellular viability of laser untreated and laser treated IDSNPs at various concentrations.*

4.8. Cellular uptake of ICG and DOX-loaded SNPs.

To examine the cellular uptake of the nanoparticles fluorescence emission study was performed for the ICG and DOX loaded nanoparticles. The cells treated with ID-SNPs exhibited the fluorescence emission of ICG shown in red from the cytoplasm and the emission of DOX shown in green from the nucleus region. Figure 4.14 shows the uptake of IDSNPs and control cells. According to Figure 4.14.F and 4.14.G. Figure 4.14.F and 4.14.G combined image is shown in Figure 4.14.H. The combined image that is overlaid demonstrates where DOX is located in the nucleus and where ICG is located inside the cell cytoplasm. The aforementioned discovery suggests that IDSNPs exhibit functional activity and efficiently transport ICG and DOX to the cells. Because of this, the ID-SNPs that are fabricated with an ultrasonic atomizer are effective at encapsulating and transporting the theranostic agents (ICG and DOX) into the cells. Therefore, ID-SNPs may also be utilised in other biomedical applications.

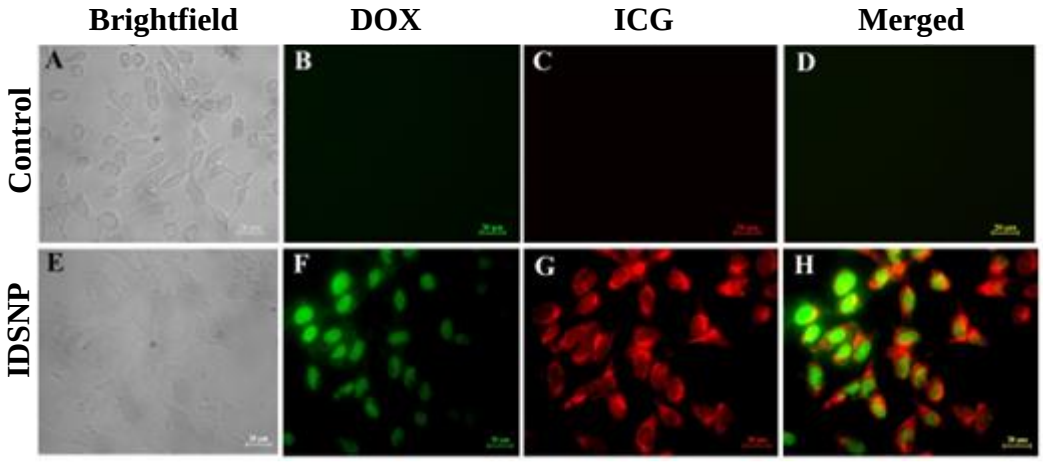

Figure 4.14 *Cellular uptake of IDSNPs treated cells.,Row1(A-D)shows the brightfield image of control i.e untreated cells , DOX emission of control, ICG emission of control and merged image of control. Row 2 (E-H) shows the brightfield image of control IDSNP treated cells , DOX emission of IDSNP treated cells, C-G emission of IDSNP treated cells and merged image of IDSNP treated cells.*

4.9. Live and Dead cell assessment of IDSNP incubated cells with laser irradiation.PI staining was performed to identify the dead cell after the laser and IDSNP-treated cells. In Figure 4.15, the control cells exhibit minimal red emission of propidium iodide (PI) in both laser-treated and untreated conditions, indicating that laser irradiation alone does not induce significant harm to healthy cells. Contrastingly, IDSNP-treated cells display elevated PI emission upon laser treatment compared to the untreated group. In the absence of laser irradiation, IDSNP-treated cells show low emission, primarily attributed to DOX presence. However, upon exposure to an 808 nm laser, a notable increase in red emission occurs, indicative of heightened cell death resulting from the synergistic effect of DOX and laser irradiation. This observation leads to the conclusion that IDSNPs serve as highly effective chemophotothermal agents, demonstrating enhanced therapeutic efficacy through combined chemotherapy and photothermal treatment

modalities.This suggests that IDSNPs are suitable for combined photothermal and chemotherapy.

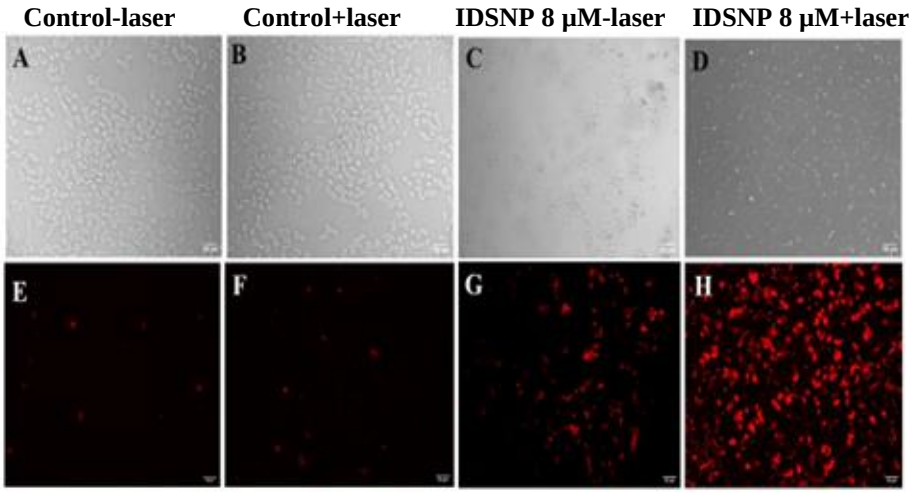

Figure 4.15 *Propidium Iodide Staining of IDSNPs treated cells , Row 1 (A-D)shows the brightfield image of control without laser, control with laser, 8 µM IDSNP treated without laser and 8 µM IDSNP treated with laser respectively. Row 2 (E-H) shows the brightfield image of PI stained control without laser, PI stained control with laser, PI stained 8 µM IDSNP treated without laser and PI stained 8 µM IDSNP treated with laser respectively.Scale bar-50µm.*

Chapter 5

Conclusion

The utilization of biocompatible and biodegradable silk fibroin nanoparticles for the dual delivery of the chemotherapeutic drug Doxorubicin (DOX) and the photothermal agent Indocyanine Green (ICG) has been thoroughly investigated in this study. Our findings demonstrate successful encapsulation of ICG within the IDSNPs, achieving a loading efficiency of approximately ~98%, attributed to J-aggregation (~851 nm) induced by DOX, far surpassing the loading capacity of nanoparticles solely loaded with ICG (~20%). This unique interaction was corroborated by the absorption and emission spectra, indicating significant structural changes in the protein nanoparticles, as evidenced by CD spectra analysis. The physicochemical characterization confirmed the increase in nanoparticle size from 70± 4 nm to 80± 4 nm upon loading with ICG and DOX, as observed in SEM imaging. Subsequent investigations into the photothermal properties revealed that the temperature rise was directly proportional to the power and concentration of the IDSNPs, with a calculated Δt of 16°C. Notably, IDSNPs exhibited greater photothermal stability compared to free ICG.

Cellular studies unveiled the superior efficacy of IDSNPs, with an IC50 value of 0.6725 ± 0.02 µM, significantly lower than that of free DOX (1.15 ± 0.02 µM) within 24 hours, demonstrating enhanced cytotoxicity against cancerous cells. Additionally, cellular uptake studies illustrated the preferential localization of DOX within the nucleus and ICG in the cytoplasm, resulting in a notable decrease in cellular viability (30%) upon IDSNP treatment followed by laser irradiation within 6 hours. This observation was corroborated by PI staining, showing reduced red emission in IDSNP-treated cells post-irradiation, indicative of cellular damage.

In conclusion, our study highlights the dual functionality of IDSNPs as effective chemotherapeutic and photothermal agents, showcasing synergistic therapeutic efficacy surpassing individual treatments. This

integrated approach holds promise for advancing cancer therapy by leveraging the combined benefits of chemotherapeutic and photothermal modalities.

Scope for future work

This project's findings will be investigated in the 3D cell culture and animal model and then after successful in vivo experiments, it can be taken to the market value with clinical trials.

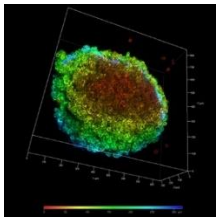

Figure 5.1. 3D cell culture. This image depicts a tumor spheroid.

Figure 5.2. In vivo experiments. This image depicts the in vivo experiments of the drug on the mice model.

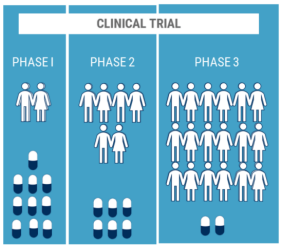

Figure 5.3. Clinical trials. This image depicts the clinical trials of the drug on human and it occurs in different phases.

References

ALTUN, İ., & SONKAYA, A. (2018). The Most Common Side Effects Experienced by Patients Were Receiving First Cycle of Chemotherapy. *Iranian Journal of Public Health*, *47*(8), 1218–1219.

Barathan, M., Vellasamy, K. M., Mariappan, V., Venkatraman, G., & Vadivelu, J. (2023). Naturally Occurring Phytochemicals to Target Breast Cancer Cell Signaling. *Applied Biochemistry and Biotechnology*. https://doi.org/10.1007/s12010-023-04734-0

Bigger, S. W., Ghiggino, K. P., Meilak, G. A., & Verity, B. (1992). Illustration of the principles of fluorimetry. An apparatus and experiments specially designed for the teaching laboratory. *Journal of Chemical Education*, *69*(8), 675. https://doi.org/10.1021/ed069p675

Chandrashekar, D. S., Karthikeyan, S. K., Korla, P. K., Patel, H., Shovon, A. R., Athar, M., Netto, G. J., Qin, Z. S., Kumar, S., Manne, U., Creighton, C. J., & Varambally, S. (2022). UALCAN: An update to the integrated cancer data analysis platform. *Neoplasia*, *25*, 18–27. https://doi.org/10.1016/j.neo.2022.01.001

Chidambaram, M., Manavalan, R., & Kathiresan, K. (2011). Nanotherapeutics to overcome conventional cancer chemotherapy limitations. *Journal of Pharmacy & Pharmaceutical Sciences: A Publication of the Canadian Society for Pharmaceutical Sciences, Societe Canadienne Des*

Sciences Pharmaceutiques, *14*(1), 67–77. https://doi.org/10.18433/j30c7d

Dearnaley, D. P., Khoo, V. S., Norman, A. R., Meyer, L., Nahum, A., Tait, D., Yarnold, J., & Horwich, A. (1999). Comparison of radiation side-effects of conformal and conventional radiotherapy in prostate cancer: A randomised trial. *Lancet (London, England)*, *353*(9149), 267–272. https://doi.org/10.1016/S0140-6736(98)05180-0

Debela, D. T., Muzazu, S. G., Heraro, K. D., Ndalama, M. T., Mesele, B. W., Haile, D. C., Kitui, S. K., & Manyazewal, T. (2021). New approaches and procedures for cancer treatment: Current perspectives. *SAGE Open Medicine*, *9*, 20503121211034366. https://doi.org/10.1177/20503121211034366

Doughty, A. C. V., Hoover, A. R., Layton, E., Murray, C. K., Howard, E. W., & Chen, W. R. (2019). Nanomaterial Applications in Photothermal Therapy for Cancer. *Materials (Basel, Switzerland)*, *12*(5), 779. https://doi.org/10.3390/ma12050779

Estelrich, J., & Busquets, M. A. (2018). Iron Oxide Nanoparticles in Photothermal Therapy. *Molecules*, *23*(7), Article 7. https://doi.org/10.3390/molecules23071567

GLOBOCAN 2020: New Global Cancer Data | UICC. (n.d.). Retrieved April 24, 2024, from https://www.uicc.org/news/globocan-2020-global-cancer-data

Hackethal, A., Hirschburger, M., Eicker, S. O., Mücke, T., Lindner, C., & Buchweitz, O. (2018). Role of Indocyanine Green in

Fluorescence Imaging with Near-Infrared Light to Identify Sentinel Lymph Nodes, Lymphatic Vessels and Pathways Prior to Surgery – A Critical Evaluation of Options. *Geburtshilfe Und Frauenheilkunde*, *78*(1), 54–62. https://doi.org/10.1055/s-0043-123937

Han, H. S., & Choi, K. Y. (2021). Advances in Nanomaterial-Mediated Photothermal Cancer Therapies: Toward Clinical Applications. *Biomedicines*, *9*(3), Article 3. https://doi.org/10.3390/biomedicines9030305

Haris, M., Yadav, S. K., Rizwan, A., Singh, A., Wang, E., Hariharan, H., Reddy, R., & Marincola, F. M. (2015). Molecular magnetic resonance imaging in cancer. *Journal of Translational Medicine*, *13*, 313. https://doi.org/10.1186/s12967-015-0659-x

He, W., Li, P., Zhu, Y., Liu, M., Huang, X., & Qi, H. (2019). An injectable silk fibroin nanofiber hydrogel hybrid system for tumor upconversion luminescence imaging and photothermal therapy. *New Journal of Chemistry*, *43*(5), 2213–2219. https://doi.org/10.1039/C8NJ05766D

Herrera Estrada, L. P., & Champion, J. A. (2015). Protein nanoparticles for therapeutic protein delivery. *Biomaterials Science*, *3*(6), 787–799. https://doi.org/10.1039/c5bm00052a

Huang, X., Jain, P. K., El-Sayed, I. H., & El-Sayed, M. A. (2008). Plasmonic photothermal therapy (PPTT) using gold nanoparticles. *Lasers in Medical Science*, *23*(3), 217–228. https://doi.org/10.1007/s10103-007-0470-x

Jaiswal, S., Roy, R., Dutta, S. B., Bishnoi, S., Kar, P., Joshi, A., Nayak, D., & Gupta, S. (2022). Role of Doxorubicin on the Loading Efficiency of ICG within Silk Fibroin Nanoparticles. *ACS Biomaterials Science & Engineering*, *8*(7), 3054–3065. https://doi.org/10.1021/acsbiomaterials.1c01616

Knijn, N., Simmer, F., & Nagtegaal, I. D. (2015). Recommendations for reporting histopathology studies: A proposal. *Virchows Archiv*, *466*(6), 611–615. https://doi.org/10.1007/s00428-015-1762-3

Li, J., Zhang, W., Ji, W., Wang, J., Wang, N., Wu, W., Wu, Q., Hou, X., Hu, W., & Li, L. (2021). Near infrared photothermal conversion materials: Mechanism, preparation, and photothermal cancer therapy applications. *Journal of Materials Chemistry B*, *9*(38), 7909–7926. https://doi.org/10.1039/D1TB01310F

Majeed, H., & Gupta, V. (2024). Adverse Effects of Radiation Therapy. In *StatPearls*. StatPearls Publishing. http://www.ncbi.nlm.nih.gov/books/NBK563259/

Mattiuzzi, C., & Lippi, G. (2019). Current Cancer Epidemiology. *Journal of Epidemiology and Global Health*, *9*(4), 217–222. https://doi.org/10.2991/jegh.k.191008.001

Melamed, J. R., Edelstein, R. S., & Day, E. S. (2015). Elucidating the Fundamental Mechanisms of Cell Death Triggered by Photothermal Therapy. *ACS Nano*, *9*(1), 6–11. https://doi.org/10.1021/acsnano.5b00021

Numata, K., Yamazaki, S., & Naga, N. (2012). Biocompatible and Biodegradable Dual-Drug Release System Based on Silk Hydrogel Containing Silk Nanoparticles. *Biomacromolecules*, *13*(5), 1383–1389. https://doi.org/10.1021/bm300089a

Perkampus, H.-H. (2013). *UV-VIS Spectroscopy and Its Applications*. Springer Science & Business Media.

Pham, D. T., & Tiyaboonchai, W. (2020). Fibroin nanoparticles: A promising drug delivery system. *Drug Delivery*, *27*(1), 431–448. https://doi.org/10.1080/10717544.2020.1736208

Power, S. P., Moloney, F., Twomey, M., James, K., O'Connor, O. J., & Maher, M. M. (2016). Computed tomography and patient risk: Facts, perceptions and uncertainties. *World Journal of Radiology*, *8*(12), 902–915. https://doi.org/10.4329/wjr.v8.i12.902

Seyfried, T. N., & Shelton, L. M. (2010). Cancer as a metabolic disease. *Nutrition & Metabolism*, *7*, 7. https://doi.org/10.1186/1743-7075-7-7

Siegel, R. L., Miller, K. D., Wagle, N. S., & Jemal, A. (2023). Cancer statistics, 2023. *CA: A Cancer Journal for Clinicians*, *73*(1), 17–48. https://doi.org/10.3322/caac.21763

Sritharan, S., & Sivalingam, N. (2021). A comprehensive review on time-tested anticancer drug doxorubicin. *Life Sciences*, *278*, 119527. https://doi.org/10.1016/j.lfs.2021.119527

Taymaz-Nikerel, H., Karabekmez, M. E., Eraslan, S., & Kırdar, B. (2018). Doxorubicin induces an extensive transcriptional and

metabolic rewiring in yeast cells. *Scientific Reports*, *8*(1), 13672. https://doi.org/10.1038/s41598-018-31939-9

Vincy, A., Bhatia, N., & Vankayala, R. (2022). Optical Characteristics of Indocyanine Green J-Aggregates Induced by Cisplatin for Phototheranostic Applications. *ACS Biomaterials Science & Engineering*, *8*(12), 5119–5128. https://doi.org/10.1021/acsbiomaterials.2c01135

Xiao, L., Lu, G., Lu, Q., & Kaplan, D. L. (2016). Direct Formation of Silk Nanoparticles for Drug Delivery. *ACS Biomaterials Science & Engineering*, *2*(11), 2050–2057. https://doi.org/10.1021/acsbiomaterials.6b00457

Zhang, Y., Zhan, X., Xiong, J., Peng, S., Huang, W., Joshi, R., Cai, Y., Liu, Y., Li, R., Yuan, K., Zhou, N., & Min, W. (2018). Temperature-dependent cell death patterns induced by functionalized gold nanoparticle photothermal therapy in melanoma cells. *Scientific Reports*, *8*(1), 8720. https://doi.org/10.1038/s41598-018-26978-1

ZhuGe, D.-L., Wang, L.-F., Chen, R., Li, X.-Z., Huang, Z.-W., Yao, Q., Chen, B., Zhao, Y.-Z., Xu, H.-L., & Yuan, J.-D. (2019). Cross-linked nanoparticles of silk fibroin with proanthocyanidins as a promising vehicle of indocyanine green for photo-thermal therapy of glioma. *Artificial Cells, Nanomedicine, and Biotechnology*, *47*(1), 4293–4304. https://doi.org/10.1080/21691401.2019.1699819

Zou, L., Wang, H., He, B., Zeng, L., Tan, T., Cao, H., He, X., Zhang, Z., Guo, S., & Li, Y. (2016). Current Approaches of Photothermal Therapy in Treating Cancer Metastasis with Nanotherapeutics. *Theranostics*, *6*(6), 762–772. https://doi.org/10.7150/thno.14988

Zugazagoitia, J., Guedes, C., Ponce, S., Ferrer, I., Molina-Pinelo, S., & Paz-Ares, L. (2016). Current Challenges in Cancer Treatment. *Clinical Therapeutics*, *38*(7), 1551–1566. https://doi.org/10.1016/j.clinthera.2016.03.026